Multiscale and Multidisciplinary Modeling, Experiments and Design
https://doi.org/10.1007/s41939-023-00162-z

ORIGINAL PAPER

Morphological evolution and strength performance of green-aluminium-7075 hybrid composites modeled by response surface analysis

Olanrewaju Seun Adesina[1,4] · Abayomi Adewale Akinwande[2] · Adeolu Adesoji Adediran[3] · Oluwatosin Abiodun Balogun[2] · Olufemi Oluseun Sanyaolu[1,4] · Valentin Romanovski[5,6]

Received: 8 November 2022 / Accepted: 3 May 2023

Abstract
In developing countries, the importation of synthetic ceramic particles for particulate reinforcement of metal matrixes is costly, so locally sourced and sustainable alternatives are sought after Rice husk ash (RHA) at 3–12 wt.%, glass powder (GP) at 2–10 wt.%, and stirring temperature (ST) at 600–800 °C were evaluated for their effects on the elemental distribution, microstructure, and tensile performance of aluminum-7075 green composite. Response surface was utilized in the experimental design and statistical analysis of the experimental results for the purpose of determining the optimal combination of the three input variables. Yield, ultimate tensile, flexural, and impact strengths, as well as microhardness and compressive strength, are examined as responses. To optimize these parameters, response surface analysis was incorporated into the experimental design, modeling, and optimization procedures. Variation in experimental variables led to microstructural evolution, which in turn caused variation in performance. Response surface analysis (RSA) revealed that the input factors contributed significantly to each response, resulting in regression models statistically suited to represent the experimental data, as confirmed by the diagnostic plots. As a consequence of the optimization, a combination of 7.2% RHA, 6.2 GP, and 695 °C with a desirability of 0.91 was deemed optimal. A comparison between the predicted values for the responses and the values from the validation experiment revealed that each response had an error < 5%. Consequently, the models are certified adequate for response prediction with a confidence level of 95%, and the optimal combination is adequate for the composite's design.

Keywords Al-7075 · Green fillers · Mechanical performance · Modeling and optimization · Response surface method

✉ Olanrewaju Seun Adesina
osaadesina@gmail.com

✉ Abayomi Adewale Akinwande
abypublications@gmail.com

1 Department of Mechanical Engineering, Redeemer's University, Ede, Osun, Nigeria

2 Department of Metallurgical and Materials Engineering, Federal University of Technology, Akure, Ondo, Nigeria

3 Department of Mechanical Engineering, Landmark University, Omu-Aran, Kwara, Nigeria

4 Industry, Innovation and Infrastructure, Redeemer's University, Ede SDG9, Osun, Nigeria

5 Center for Functional Nano-Ceramics, National University of Science and Technology, "MISIS", Lenin Av., 4, 119049 Moscow, Russia

6 Department of Materials Science and Engineering, University of Virginia, Charlottesville, VA 22904, USA

1 Introduction

The increasing production and disposal of waste has been a major source of concern globally. Wastes are produced on a daily basis and their sources include municipal, industrial, agricultural, and many others. As long as there is human existence, unwanted waste materials will continually be produced, and with the increasing world population, the production of these wastes is on the uptrend, birthing more challenges in managing the waste. The challenge has brought concerned individuals and organizations to devise means and ways of managing disposed wastes with the view of reducing their environmental impact. As a way of maintaining a healthy environment, several activities have been geared toward reducing unwanted materials by recycling them into other useful components (Tripathi et al. 2020; Akinwande et al. 2022a, 2021). By these means, eco-friendly materials and components are designed to meet one or two human

Published online: 03 June 2023

needs. Furthermore, recycling is a way in which unwanted or waste materials are given economic importance, bringing about the concept of "waste to wealth". Several studies have alluded to the fact that incorporation of waste as part of developed engineered components has resulted in cheaper and ecofriendly "green" products (Akinwande et al. 2022b, 2022c; Adediran et al. 2022, 2021a).

Nowadays, metal matrix composites are being incorporated with waste-derived reinforcements for the purpose of producing lightweight engineering parts (Nandy et al. 2022; Bulei et al. 2019). Automobiles, for instance, are now being designed to be light to optimize fuel consumption. In that case, the design of automobile parts and components is conceived to involve lightweight materials. Aluminum (Al) and its composites are kinds of metal matrix desired for the design of vehicles on account of their lighter weight as compared with steel, which has been used in the past (Kumar et al. 2023; Dwivedi et al. 2016). Parts of vehicles like the outer and inner panels, passenger compartment, hoods, front and rear doors, structural panels, and many more are in most cases made with aluminum alloys (Hirsch 2011, 2014). To further improve the strength of aluminum parts, even in automobiles, researchers have utilized ceramic reinforcement like SiO_2, TiO_2, WC, B_4C, SiC, AlN, TiS_2, NbC, MoN, Al_2O_3, ZrO_2, and many others in aluminum alloy matrix (AAM) (Ogunsanya et al. 2023; Bian et al. 2020; El-Mahallawi et al. 2015; Kumar et al. 2022a, 2022b). Even particles like that of cobalt, chromium, manganese, nickel, vanadium, tantalum and others have been engaged in the strengthening and modification of aluminium alloys (Kumar et al. 2022c, 2010; Abraham et al. 2019).

Achievement has been made in terms of strength improvement. However, going by their densities, their incorporation in AAM has resulted in a heavy weight aluminum composite. The densities of the listed reinforcements are greater than 2.7 g/cm^3, hence, are heavier than aluminum. Furthermore, accessing these resources is quite expensive for researchers in developing countries (Selvam et al. 2021; Myalska-Glowacka et al. 2022).

Alternatively, waste-derived reinforcements, whether municipal, industrial, or agro-wastes, are lighter in weight than synthetic ceramic reinforcement. They are also cheaper and greener (owing to recycling). For instance, calcined powders in the form of rice husk, palm kernel shell, bamboo leaf, coconut shell, egg shell, snail shell, to mention but a few, possess densities of 0.31, 0.745, 0.36, 0.45, 0.81, and 0.54 g/cm^3 respectively. The materials are lighter than both the ceramic reinforcement and the aluminum alloy itself (Sydow et al. 2021; Hayajneh et al. 2019). Discoveries have shown that these waste-derived powders, tagged "green fillers" (based on their sources), contain some constituents of the initially mentioned ceramic particles like silica and alumina (Ikubanni et al. 2020; Adesina et al. 2023). It therefore means the addition of the "green fillers" not only possesses the potency of improving the properties of the aluminum alloy matrix but also produces a lightweight composite suitable for lightweight engineering applications. The green fillers are also sustainable and cheaper. Hence, their engagement in reinforcing aluminum alloy in producing stronger and lighter alloys is well justified.

Past literature on the development and utilization of "green fillers" in aluminum matrix reported interesting outcomes. In the findings showcased by Mishra et al. (Mishra et al. 2017), the hardness of aluminum LM-6 alloy was improved. Udoye et al. (Udoye et al. 2020) found that infusing 2–8% rice husk ash into aluminum 6061 melt increased tensile strength by 16.5% and hardness by 33.3%. In the same manner, Gladston and his team improved the tensile and hardness performance of aluminum 6061 with rice husk ash at 8% maximum content (Gladston et al. 2015a). An investigation conducted by Saravanan and his team affirmed the contribution of rice husk ash as a good reinforcing green filler (Saravanan et al. 2013). In their report, 3–12% of the filler was introduced into AlSi10Mg matrix, with the consequence of enhancing the hardness, with maximum value attained at a 12% dose.

Other green fillers reported in the literature are palm kernel shell and coconut shell ashes. Edoziuno et al. (Edoziuno et al. 2021) blended palm kernel shell ash in an aluminum 6063 matrix in proportions of 2.5, 5.0, 7.5, 10.0, 12.5, and 15% wt. From the outcome, dosage of 2.5–7.5 wt.% addition resulted in a boost in tensile strength parameters, while 10, 12.5 and 15 wt.% kindled consecutive decreases. It was further disclosed that peak hardness and impact strength were attained at 2.5 and 10 wt.%, respectively. Panda et al. (Panda et al. 2020) infused coconut shell ash in aluminum-1200 alloy and found a 19.9% increase in hardness at 4% ash content. Al-12%Si matrix was imbued with melon ash content in proportions of 5, 10, 15, and 20%. The ash was revealed to boost hardness and tensile strength with maximum attainment at 15 wt.%. Ceramic green fillers derived from agrowaste have also been injected in hybrid aluminum composites as a supplement to synthetic fillers (Kolappan et al. 2022; Kulkarni and Siddeswarappa 2022; Subramaniam et al. 2018; Imran et al. 2016). Some review studies have revealed the role of green particulates derived from agrowaste as fillers in Al alloy. The reports portrayed the immense beneficial potential inherent in these fillers in improving aluminum composites (Kulkami et al. 2019; Pareez et al. 2021; Adeleke et al. 2021).

Reinforcing fillers derived from industrial wastes or by-products like fly-ash, waste glass, marble dust, red mud, and granite dust waste have been reused in aluminum alloys. Lei (Lei 2012) researched on waste glass powder in aluminum composites. The findings showed improvement in the hardness of the aluminum composite synthesized with highest hardness value attained at 10 wt. % for sizes 75–150 micron and 15 wt. % for sizes 150–240 micron. Hendronursito et al.

(Hendronursito et al. 2020) carried out an optimization procedure on an aluminum composite reinforced with glass powder. Particulate proportion, particulate size, and stirring time were investigated. Optimum tensile strength was realized when 13% glass particulate of a particle size range of 20–80 micron was employed as filler at 30 s stirring times. Equally, Balogun et al. (Balogun et al. 2022a) examined glass particle proportion and particle size effects on the hardness and tensile properties of aluminum 6061 alloy. The proportions were varied at 2, 4, 6, 8, and 10 wt.%, and the sizes were varied at − 6, − 13, and − 23 micron. The account exhibited a boost in hardness with a rising proportion of the glass powder. Furthermore, the finest particle proportion outperformed the other particle sizes. In the case of tensile strength, peak strength was attained for the 13 and –23-micron sizes at 6 wt. %, while the finest size, 6 µm, yielded optimum tensile strength at 8 wt. %. Other green fillers derived from industrial wastes and by-products are fly ash (Bharathi et al. 2017; Sharma et al. 2017; Gikunoo et al. 2013; Boopathi et al. 2013), red mud (derived from industrial production of aluminum) (Chinta et al. 2018; Krupakara and Ravikumar 2015), granite dust (Pai et al. 2015; Satyanarayana et al. 2019; Saini and Singh 2022), and marble dust (Kumar et al. 2021; Gangwar et al. 2019). According to the findings of the researches, industrial waste plays an important role in the reinforcement and development of lightweight and green aluminum alloys.

Processes involved in the production of aluminum composites are stir casting, vacuum stir casting, squeeze casting, friction stir process, powder metallurgy, and others (Anyalem 2020a; Arunachalam et al. 2019; Kumar et al. 2022d; Kumar and Kumar 2022). Stir casting is adopted in this study on account of its lower cost of operation and ability for mass production. In our previous studies (Akinwande et al. 2022d), waste glass and rice husk were reprocessed into glass powder and rice husk ash and introduced into aluminum melt via the stir casting process. Casting was done at a constant temperature of 750 °C and a stirring speed of 500 rpm was employed while stirring time was 10 min. Sample preparation was carried out in group mixes A, B, C, and D. Each group mix was made with a different dosage of glass powder ranging from 2 to 10 wt.% in 2 wt.% increments. Furthermore, group mixes A, B, C, and D were blended with 3, 6, 9, and 12 wt.% rice husk ash. The findings revealed the mechanical properties were enhanced by the blend between the two additives, indicating that the two contributed significantly to the mechanical properties of the developed composites. This shows that a hybrid aluminum composite could be developed with the duo of glass powder and rice husk ash. Also, in previous studies (Adediran et al. 2021b; Balogun et al. 2022b; Ogunsanya et al. 2022), TiO_2 was adopted as a reinforcing additive in the matrixes of aluminum alloy. For the sake of sustainability and owing to the high cost of procuring TiO_2 in developing countries, the present research was conceived to employ locally sourced materials as green fillers in Al-7075. In (Akinwande et al. 2022d), the stirring temperature was maintained at 750 °C. Based on the nature of the investigation, there was no way the stirring temperature was ascertained to be an optimum temperature. A temperature range of 600–800 °C is therefore adopted in the present study for the purpose of investigating a relatively moderate temperature for the casting process. This study involves investigation with waste glass and rice husk ash as alternative fillers in Al 7075 composite toward developing a green-hybrid-aluminium-7075 composite. These green fillers are cheaper, and sustainable, hence, report accessed sustainable green fillers as cheaper alternative to imported synthetic fillers. Via this means, aluminum composite can be improved using locally sourced additives, thereby conserving money and reducing importation. Furthermore, there are few studies that considered the combination of agro-based and industrial by-products in the development of hybrid aluminum alloy. Therefore, this study broadens knowledge as to the development of hybrid aluminum composites employing agro-based and industrial by-products as reinforcing agents.

2 Experimental program

The experimental program entails the design of experiment, material preparation and composite development, property and microstructural evaluation, and result analysis.

2.1 Design of experiment

The design of the experiment was done by applying the Box Behnken design of the response surface method. Variable factors are rice husk ash dosage (A), glass powder (B), and stirring temperature (C). The response surface method examines the interactions that exist between variable factors and each response using mathematical and statistical approaches (Ogunbiyi et al. 2023; Akinwande et al. 2023a, 2023b). Design expert 13 was utilized in the design of the experiment and analysis of the results. Fourteen (14) experimental runs were obtained for each response parameter and evaluated. Table 1 indicates the levels of the factors for the

Table 1 levels of factors in the design of experiment

Factors	Low level	Medium level	High level
Rice husk ash (A)	3	7.5	12
Glass powder (B)	2	6	10
Casting temperature (°C)	600	700	800

Table 2 Variable distribution in the design of experiment

Experimental runs	Coded levels			Variable combination		
	A	B	C	A (wt. %)	B (wt. %)	C (degree C)
1	1	0	− 1	3	2	700
2	− 1	1	0	7.5	2	800
3	− 1	0	1	3	10	700
4	− 1	0	− 1	7.5	10	600
5	1	0	1	12	6	800
6	0	− 1	1	7.5	6	700
7	0	0	0	7.5	2	600
8	0	0	0	12	10	700
9	0	− 1	− 1	3	6	800
10	0	1	− 1	12	6	600
11	− 1	− 1	0	12	2	700
12	1	1	0	7.5	6	700
13	0	0	0	7.5	10	800
14	1	− 1	0	3	6	600

A is rice husk ash proportion, B is glass powder dosage, C is casting temperature

design of the experiment, and Table 2 presents the combination of the experimental variables.

2.2 Material preparation

An aluminum 7075-T6 ingot (chemical composition indicated in Table 1) was procured for the experiment. Glass powder was prepared by breaking collected waste glass into smaller pieces, followed by grinding and milling into powder. Glass powder screened to a 23 µm pass was collected in a container for the experimental procedure. The obtained rice husk was washed under running water and dried in the open air for 48 h before being heated in a muffle furnace at 700 ˚C for 6 h. The ash realized was broken into pieces and further milled. Rice husk ash screened to -23 µm was employed in the process. Casting was done in a graphite crucible of dimensions (100 mm in diameter and 175 mm in height).

2.3 Development of green Al-7075 composites

The experimental design for the composites as regards particulate mixture and casting temperature was effected according to the dictates of Table 2. The crucible and the green fillers were preheated to 500 °C before charging in the Al-7075 ingot. The temperature was raised to stipulated temperatures (Table 2). The melt was stirred at 300 rpm and preheated fillers were charged into the vortex created. The discharge rate for the fillers was maintained at a rate of 2.5 g/min. Stirring was done at 300 rpm for 10 min for each mix. Afterwards, the liquid melt of the composites was discharged into metal molds at a 2.4 cm^3/s pouring rate. The solidification rate was maintained at 100 K/s.

2.4 Property evaluation

Samples sectioned to 10 × 10 × 10 (mm^3) were mounted into epoxy resin for easier handling during grinding and polishing. Abrasive papers (120–240 grit) were used in the surface grinding process and polishing of the samples' surface via abrasive paper of 800 and 1200 grit. At the end, mirror-like surfaces were obtained. The polished surface was then swabbed for 30 s with Kroll's solution as etchant after which the surfaces were rinsed with distilled water and dried via a laboratory dryer for one minute. The samples were subjected to microstructural examination with the aid of scanning electron microscope (JSM-7610F) equipped with an energy dispersive spectrometer attachment (EDS AZ-tec) for elemental composition analysis. Inherent phases of the samples were accessed by employing ADX8000 (ANGSTROM) X-ray diffractometer. At two theta angles varying from 0 to 100˚, the phases were analyzed.

For the tensile test, samples were initially machined to a dog-boned shape of length 120 mm, a gage length of 60 mm, and a gage diameter of 10 mm according to the ASTM E 8/E8M-21 (ASTM E 8, E8M-21 2021) procedure. A tensile test was carried out on the machined samples via a universal testing machine (Instron 3369 Series) and, from the results obtained, yield and ultimate tensile strength were estimated. Samples were tested in triplicates. Flexural strength was examined in line with ASTM A 370 (ASTM A 370–20 2020). on samples of dimensions of 100 mm × 10 mm ×

10 mm via a three-point bending approach and estimated employing Eq. 1. A sample of diameter 40 mm and length 20 mm was employed for the Vickers microhardness test. The surfaces of the samples were polished and a load of 10N was applied for 10 s, and six different indentation points were chosen and average values were reported (ASTM E 384–11) (ASTM E 384–17 2017). Izod impact strength was measured on samples (100 mm × 10 mm) notched at 60˚ with a 30 kg pendulum. Impact energy absorbed up to fracture was noted. A field emission scanning electron microscope (JSM-7610 E) was used in examining the microstructure of developed composites according to ASTM E 3–11 (ASTM E 3–11 2017). Developed composites (machined to 8 mm in diameter and 16 mm in length) were subjected to quasi-static compressive loading as per ASTM E09-9 (ASTM E 9–09 2018) using the universal testing machine. A compressive load of 100KN was applied at a strain rate of 10^{-3}/s. Compressive strength was obtained as the ratio of failure load to cross-sectional area.

$$FS = 3Ly/2xh^2 \quad (1)$$

where FS is flexural strength (MPa), L is applied load (N), y is the length of the sample (mm), x is the width (mm), and h is the thickness (mm). A Scanning electron microscope (TM 3030) accompanied by energy dispersive X-ray spectroscopic accessories was used for the microstructural characterization.

3 Results and discussion

Obtained results are presented and discussed.

3.1 Properties of input materials

The elemental composition by energy dispersive spectrometer (EDS) for the ingot is portrayed in Fig. 1. Aluminium is the major element with the highest peak. The presence of zinc and magnesium in the stipulated proportion indicates it's an Al–Mg-Zn alloy (Mukherjee et al. 2015). Meanwhile, minor elements are Fe, Si, and Mn. The properties of the alloy are listed in Table 3. They are 2.79 g/cc density, 119 HV microhardness, 421 MPa yield strength, 505 MPa ultimate tensile strength, 415 MPa flexural, 4.82 kJ/m^2 impact strength, and 394 MPa compressive strength.

The chemical composition of glass powder (GP) and rice husk ash (RHA) fillers is showcased in Table 4. SiO_2 is the major compound in GP, a very useful additive for reinforcement of Al alloy (Joseph and Babaremu 2019). The chemical compositions of the RHA are presented in Table 4. SiO_2 takes the largest share of the chemical composition with a value of 90.21% by which it can be deduced the RHA is basically silica base (Table 5).

3.2 Property responses of composites

3.3 Interaction between filler count and stirring temperature on diffraction patterns, elemental distributions and microstructure of prepared composite specimen.

3.3.1 Composites prepared at 600 ˚C

Four specimens (by composition) were prepared at 600 °C as dictated by the experimental runs indicated in Table 2. For experimental runs 4, 7, 10, and 14, the compositions are 7.5% RHA/10% GP; 7.5% RHA/2% GP; 12% RHA/6% GP; and 3% RHA/6% GP in that order. For the purpose of proper reference to the mix proportions, the specimens are labeled after the composition. For example, for experimental run 4, a mix proportion of 7.5% RHA and 10% GP was prepared at 600 ˚C. As a result, the composition was designated as specimen 7.5/10/600, indicating that it contained the blend of 7.5% RHA and 10% GP and was prepared at 600 ˚C. In the same manner, specimens 7.5% RHA/2% GP; 12% RHA/6% GP; and 3% RHA/6% GP are designated as 7.5/2/600, 12/6/600, and 3/6/600, respectively. The filler count (FC %) was obtained on the addition of RHA and GP content. Arranging the specimen in the order of increasing filler counts (FC%) we have 3/6/600, 7.5/2.600, 7.5/10/600, 12/6/600 yielding respective FC % of 17.5, 9.5, 18, and 9%.

The X-ray diffraction pattern for composites prepared at 600 °C is indicated in Fig. 2. Figure 2a,b,c, and d indicate the diffraction patterns in specimens labeled 3/6/600, 7.5/2/600, 7.5/10/600, and 12/6/600, respectively. Al (matrix) and SiO_2 are the most prominently identified peaks. The Al phase was identified with the highest peak being the matrix. The SiO_2 phases identified are as a result of the silica-based reinforcement introduced into the melt. It is observed that there are

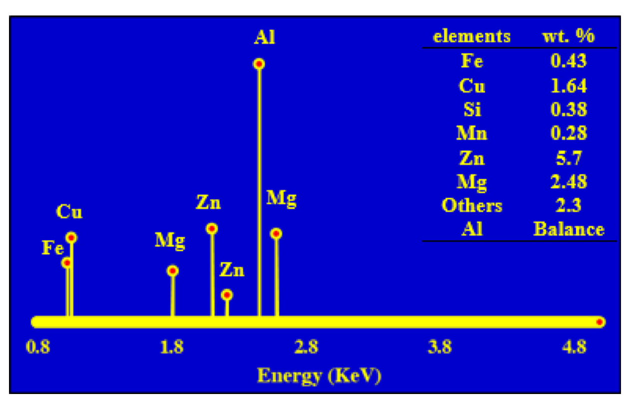

Fig. 1 Elemental composition of Al 7075

Table 3 Property of the as-received Al-7075

Density	Microhardness	Yield strength	Ultimate tensile strength	Flexural strength	Impact strength	Compressive strength
2.79 g/cc	119 HV	421 MPa	505 MPa	415 MPa	4.82 kJ/m^2	394 MPa

Table 4 Chemical composition of input materials

Materials	SiO_2	MgO	Al_2O_3	Fe_2O_3	CaO	K_2O	P_2O_5	MnO_2	Na_2O	Other
GP	74.5	1.80	4.82	0.19	7.71	0.24	0.01	0.08	8.60	2.50
RHA	90.21	0.67	0.28	0.59	0.32	2.1	0.08	0.00	0.01	5.75

Table 5 Corresponding responses realized at variable combinations and temperature

Experimental runs	Variable combinations				Responses					
	A (wt. %)	B (wt. %)	C (° C)	Designation	YS	UTS	FS	HD	IS	CS
1	3	2	700	3/2/700	400	450	134	458	5.52	352
2	7.5	2	800	7.5/2/800	397	440	136	360	4.49	308
3	3	10	700	3/10/700	405	456	184	318	4.48	550
4	7.5	10	600	7.5/10/600	402	450	162	365	5.54	596
5	12	6	800	12/6/800	260	314	181	348	4.06	312
6	7.5	6	700	7.5/6/700	610	697	177	550	7.54	606
7	7.5	2	600	7.5/2/600	502	552	127	410	6.49	396
8	12	10	700	12/10/700	255	306	205	320	3.00	600
9	3	6	800	3/6/800	404	449	162	351	4.51	252
10	12	6	600	12/6/600	350	398	156	406	4.83	392
11	12	2	700	12/2/700	350	401	162	360	4.03	400
13	7.5	10	800	7.5/10/800	307	354	195	314	3.52	497
13	7.5	6	700	7.5/6/700	608	712	178	547	7.53	610
14	3	6	600	3/6/600	497	446	135	406	6.48	346

A is rice husk ash proportion, B is glass powder dosage, C is casting temperature, YS is the yield strength (MPa), UTS is the ultimate tensile strength (MPa), FS is flexural strength (MPa), HD is microhardness (Hv), IS is impact strength (MPa), CS is compressive strength (MPa)

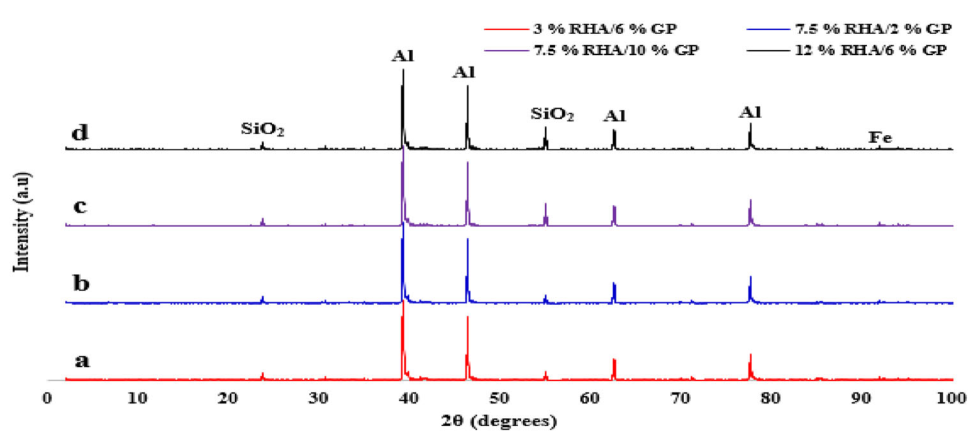

Fig. 2 X-ray diffraction patterns for composites cast at 600 ˚C and prepared with (**a**) 3% RHA/6% GP (**b**) 7.5% RHA/2% GP (**c**) 7.5% RHA/10% GP (**d**) 12% RHA/6% GP

lower peaks of SiO_2 phases in Fig. 2 a and b compared with Fig. 2c, d owing to the increasing volume of the reinforcing particles in tandem with observations of Shaikh et al. (Shaikh et al. 2019). The X-ray diffraction plot shows little or no presence of an intermetallic phase.

Figure 3a indicates the SEM image of specimen 3/6/600 (cast at 600 °C and reinforced with with 3% RHA and 6% GP). The image represents the dispersion of RHA and GP in the matrix. Even at that, there exist clusters of particulates serving as stress risers in the matrix. This is attributed to difficulty in the dispersion of the particles by the dint of lower viscosity. Akinwande et al. (Akinwande et al. 2022e) reported the same observation in aluminum 6061 reinforced with waste glass for specimens prepared at 500 °C, attributable to lower stirring temperature. Clustering is effected by a mechanism of increased interaction between particles. Also, the higher settling velocity of particles due to dispersion velocity is another reason for the observation (Canakci et al. 2014). Pores are also identified in the matrix associated with absorbed gas due to solidification shrinkage (Moses et al. 2016).

Figure 3b represents the morphological image of specimen 7.5/6/600 prepared with 7.5% RHA/6% GP at 600 °C (filler count is 13.5%). Particle clusters are identified in the matrix, imputable to the low viscosity of the melt. Clusters of RHA and GP particles are also observed in Fig. 3c for specimens 7.5/10/600 and 12/10/600. The filler counts for specimens 3/6/600, 7.5/2/600, 7.5/10/600, and 12/6/600 are 9.0, 9.5, 17.5, and 18% in that order. It is observed in Fig. 3a–d that particle clustering sites increased with rising filler counts. The formation of clusters is majorly ascribed to the lower viscosity of the melt, which prevented uniform dispersion of particles. Equally, particle clustering can be traced to higher particle density as compared with the melt. Comparing property values (Table 4) at different particulate proportions for specimens prepared at 600 °C, specimen 7.5/2/600 (filler count of 9.5%) performed better than specimen 3/6/600 (filler count of 9%) as regards yield strength (YS), ultimate tensile strength (UTS), flexural strength (FS), and impact strength (IS). Though specimen 7.5/2/600 (filler count of 9.5%) showed more clustering than specimen 3/6/600, it performed better because of the higher proportion of RHA which is lighter than GP. Refs Akinwande et al. 2022d; Gladston et al. 2015b; Saravanan and Senthilkumar 2014) had shown that at lower viscosity, heavier fillers have higher tendency to agglomerate in matrix than lighter fillers. This is because lighter RHA particles have a higher tendency to disperse within the melt than heavier GP because of the lower density of RHA. The cause of particle clustering is on account of the initial solidification of aluminum dendrites, after which there is ejection of excess particulates from the solid–liquid interface. The particles are then segregated into the inert-dendritic region. At lower viscosity, lighter particles have the tendency to be absorbed while heavier particles have a greater likelihood of being segregated due to uneven dispersion. Moreover, owing to the light weight, RHA particles possess a higher surface area and, hence, an easier tendency to be assimilated into the matrix.

It is noted that of all the four-specimens prepared at 600 °C, specimen 7.5/2/600 depicted the highest property value for yield strength, ultimate tensile strength, flexural strength, and impact strength. Specimen 7.5/10/600 (filler count 17.5%) exhibited the highest values for microhardness and compressive strength. The feat is first associated with an increase in particle volume in the melt, overshadowing the effect of clustering. It is also associated with a high amount of strain energy initiated at the particle boundaries. That is, higher filler count or particle density entails higher strain energy at the particle boundary, contributing to hardness. Vijaya et al. (Vijaya et al. 2021) and Shreyas et al. (Shreyas et al. 2021) present research on hybrid aluminum composites that confirm increasing hardness with increasing filler count. The higher compressive strength expressed by specimen 7.5/10/600 at 600 °C over other samples can be hinged on the higher density of GP in the matrix, contributing to densification with a resultant effect on the compressive strength.

Table 6 presents the elemental distribution values for the matrices of specimens labeled 3/6/600, 7.5/2/600, 7.5/10/600, and 12/6/600. The elemental composition analysis of the matrices revealed that the main elements were Al (the matrix), Si, Zn, Mg, and Cu. Compared with the base alloy (Fig. 1), Si had a higher proportion in the composites than the base alloy (Fig. 1). That confirmed the presence of the reinforcement, which was responsible for the increment in Si content. As noted, there is no appreciable difference in the elements for specimens 3/6/600 and 7.5/2/600 owing to no significant difference in the filler count. However, increasing filler count in specimens 7.5/10/600 and 12/6/600 revealed an appreciable difference in Si and Mg content, buttressing the fact that the reinforcement additives have a significant role in the elemental composition at various dosages.

Elemental analysis of spots labeled 1, 2 in Fig. 4a–d identifies the presence of Si and [O] majorly, as indicated in Fig. 6a, b. This confirms the spot to be a distribution of silica derived from RHA and GP. Spots 3 and 4 are spots of agglomeration of particles. The spot EDS results identify major elements as Si, Al, O and others as Mg, Ca, Al, and Na (Fig. 4c, d). This indicates the presence of silica, majorly affirming spots 3 and 4 in Fig. 4a–d as areas of particle agglomeration. Accordingly, the XRD results (Fig. 4a–d) identified no intermetallic phase in the composite, and also spots 3 and 4 are not intermetallic regions but rather regions of particle agglomeration.

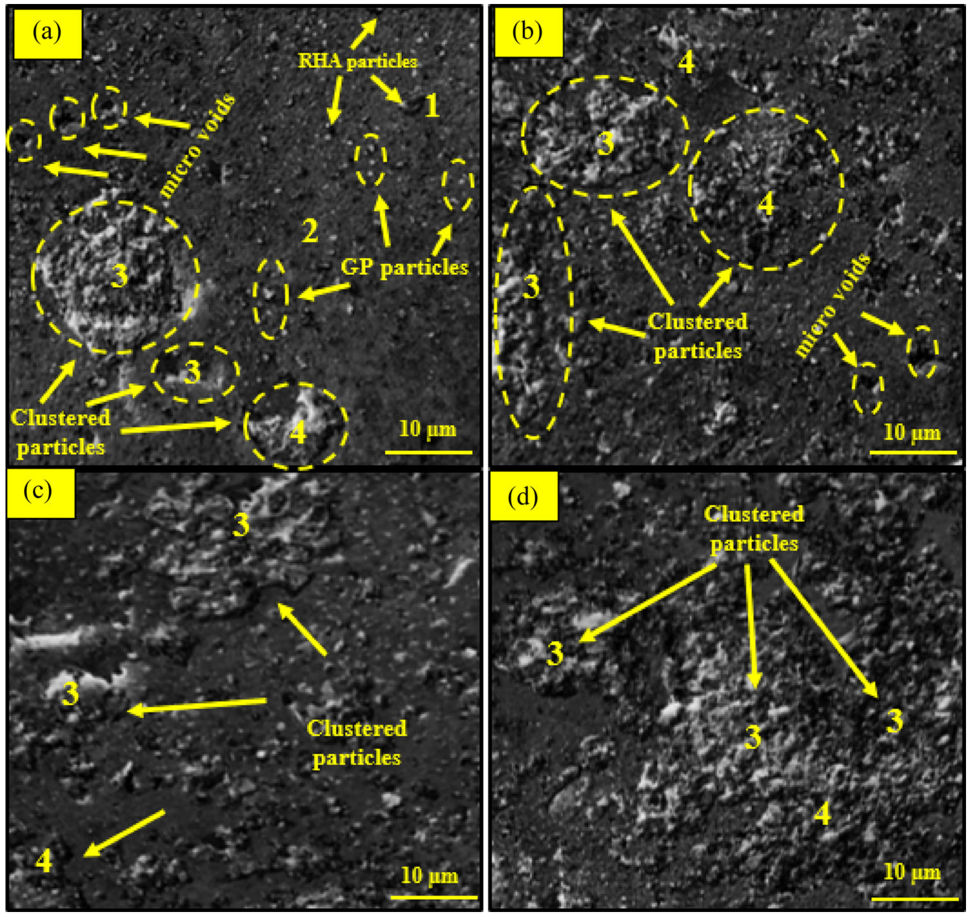

Fig. 3 FESEM morphological image of specimen cast at 600 ˚C and prepared with (**a**) 3% RHA, 6% GP (**b**) 7.5% RHA, 2% GP (**c**) 7.5% RHA, 10% GP and (**d**) 12% RHA, 6% GP

Table 6 Elemental distribution in samples cast at 600 ˚C

Specimen	FC %	Si	Zn	Mg	Cu	Fe	Mn	Other	Al
3/6/600	9.0	1.12	5.75	2.39	1.64	0.59	0.28	2.45	Balance
7.5/2/600	9.5	1.14	5.75	2.37	1.65	0.59	0.28	2.51	Balance
7.5/10/600	17.5	3.53	5.76	3.25	1.64	0.54	0.27	3.48	Balance
12/6/600	18.0	3.56	5.74	3.38	1.64	0.51	0.27	3.54	Balance

3.3.2 Composites prepared at 700 ˚C

Similar to specimens produced at 600 °C, specimens prepared at 700 °C are labeled after their composition. For experimental runs 1, 3, 6, 13, 11, and 8, specimens prepared with 3% RHA/2% GP, 3% RHA/10% GP, 7.5% RHA/6% GP, 12% RHA/2% GP, 12% RHA/10% GP are labeled 3/2/700, 3/10/700, 7.5/6/700, 7/6/700, 12/2/700, and 12/10/700 with filler counts of 9.0, 13.0, 13.5, and 22.0 respectively.

The X-ray diffraction of composites cast at 700 °C is depicted in Fig. 5. Six specimens were prepared at that temperature according to the experimental runs in Table 2. Peaks identified are Al and SiO_2. Based on the based matrix, SiO_2 peaks occur as a result of the reinforcing agents, which are silica based. As observed, the SiO_2 phase increased with increasing particulate count on account of the increasing reinforcing phase. No intermetallic content is identified in the phases highlighted in Fig. 5. The morphology of the composites prepared at 700 ˚C is portrayed in Fig. 6.

Figure 6a depicts the morphology of specimen 3/2/700 (filler count 5%), which contains 3% RHA and 2% GP. The microstructure revealed sparsely dispersed particles within the matrix. As a result, there exist some inherent matrix voids. Figure 6b depicts the microstructure of specimen 3/10/700 (filler count 13%). It is revealed that the particles are evenly dispersed when compared with specimen 3/2/700. Relative to specimen 3/2/700, specimen 3/10/700 performed better in yield strength and ultimate tensile strength marginally.

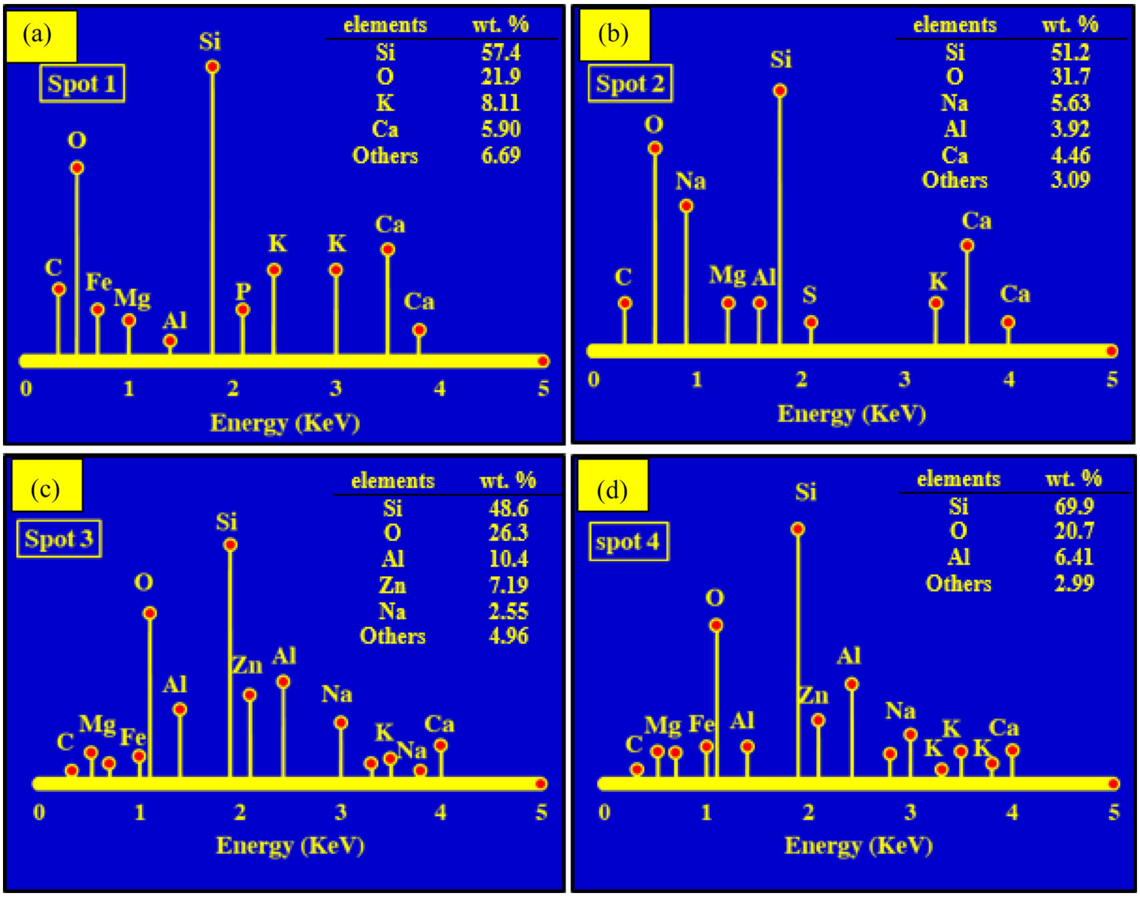

Fig. 4 Spot EDS elemental results on specimen cast at 600 ˚C prepared with (**a**) 3% RHA/6% GP (**b**) 7.5% RHA/2% GP (**c**) 7.5% RHA/10% GP and (**d**) 12% RHA/6% GP

Fig. 5 X-ray diffraction patterns for composites cast at 700 ˚C and prepared with (**a**) 3% RHA/2% GP (**b**) 3% RHA/10% GP (**c**) 7.5% RHA/6% GP (**d**) 7.5% RHA/6% GP (**e**) 12% RHA/2% GP (**d**) 12% RHA/10% GP

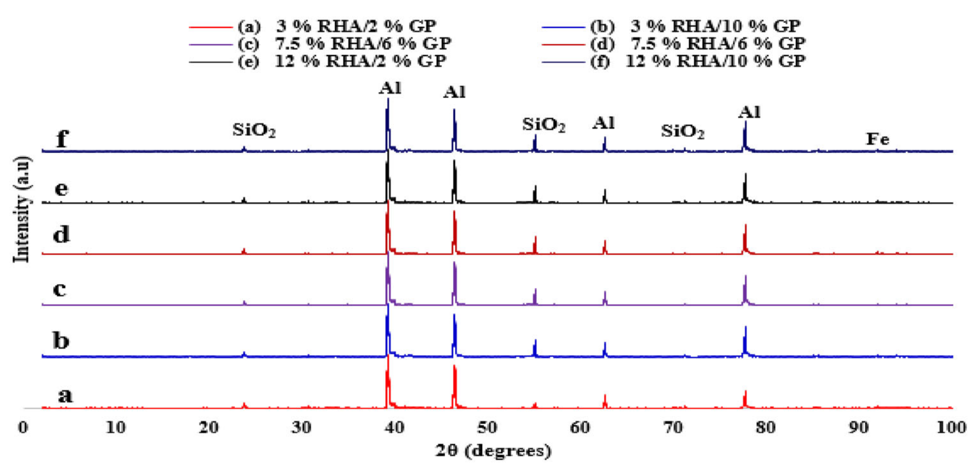

For hardness and compressive strength values, specimen 3/10/700 performed better significantly. Two reasons can be attached to this, the first of which is the higher particle density based on the higher filler count. Second, there is wider dispersion of the particles within the matrix, the consequence of which is increased particle–particle interaction. Adediran et al. (ASTM E 9–09 2018) found that 10% GP achieved maximum hardness in their study. A comparison of impact strength between the two parameters revealed that the impact strength of specimen 3/10/700 is lower than the value obtained for specimen 3/2/700 owing to the brittle nature of GP and its effect in lowering impact strength, as demonstrated by Adediran et al. (ASTM E 9–09 2018), who found that progressive addition of GP from 2 to 10% (in steps of

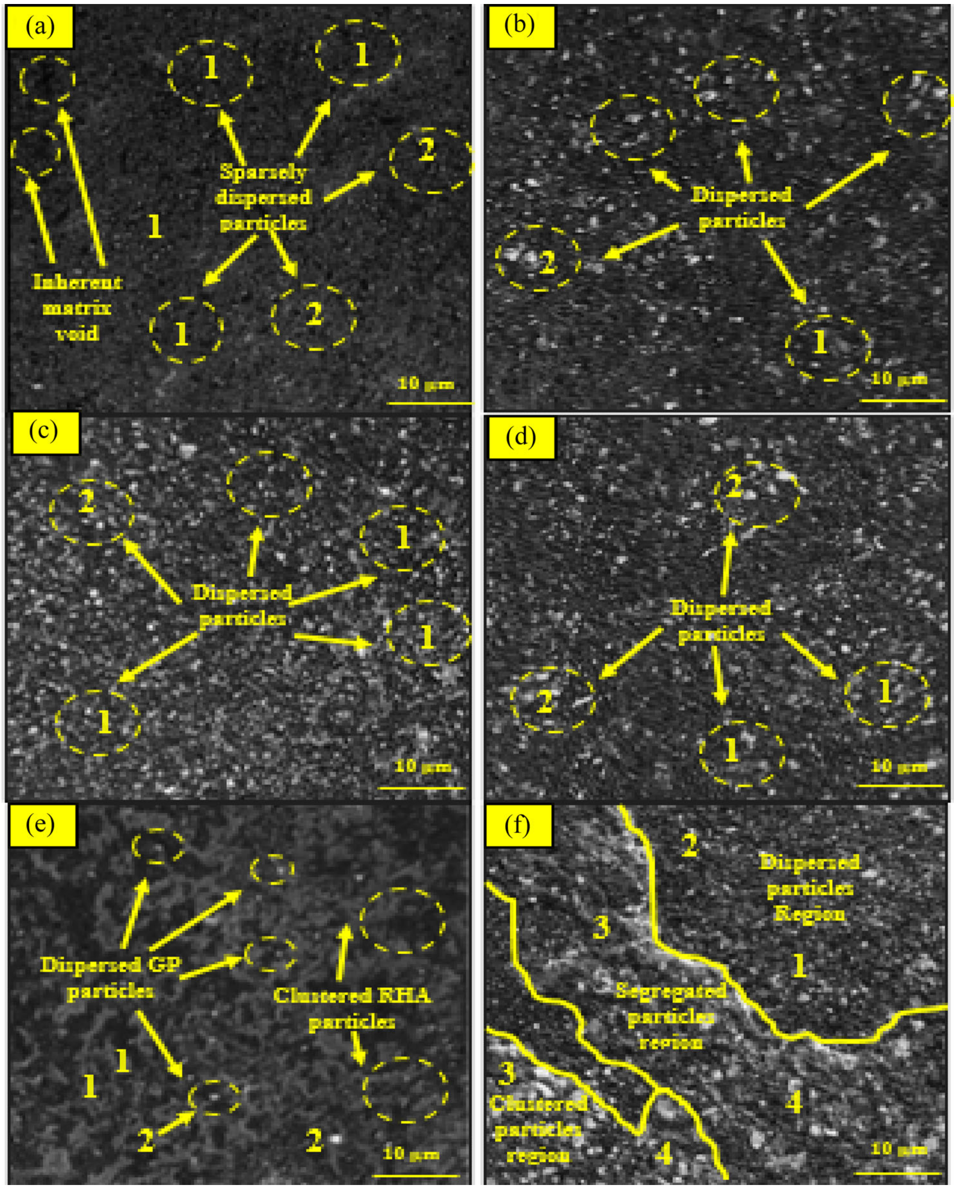

Fig. 6 FESEM morphological image of specimen cast at 700 °C and prepared with (**a**) 3% RHA/2% GP (**b**) 3% RHA/10% GP (**c**) 7.5% RHA/6% GP and (**d**) 7.5% RHA/6% GP (**e**) 12% RHA/ 2% GP (**f**) 12% RHA/10% GP

2) resulted in a progressive reduction in impact strength. The same can be explained for flexural strength.

Figure 6c, d are identified as specimens 7.5/6/700c and 7.5/6/700d, respectively, because they contained the same dosage of RHA and GP as well as the same filler count of 13.5%. In the microstructure, the particles are dispersed uniformly within the matrix. At moderate temperatures, the viscosity is receptive to the dispersion of particulates within the melt. This is evident in this study as regards the microstructure of specimens 7.5/6/700c and 7.5/6/700d. No defect is observed even as porosity is reduced. As a result of this even dispersion, the inter-particle distance was reduced and there was effective load transfer from the matrix to the reinforcement. Hence, strengthening the interfacial bonding between the matrix and the reinforcement particle. Also, pores or voids were closed up, and this resulted in improved mechanical properties of the material. Comparing the property values of 7.5/6/700c and 7.5/6/700d, there is no significant difference.

In Fig. 6e, the morphology of specimen 12/2/700 (filler count = 14%) indicates dispersion of GP and clustering of RHA. The clustering can be on the ground of a higher volume of RHA in the melt during solidification. Since RHA is light, 12 wt.% will require a large volume result, which triggers clustering as showcased in the morphology. The cluster points serve as stress risers, inducing a reduction in strength. The effect can be further explained by the reduced property value for specimen 12/2/700 when compared with specimen 7.5/6/700. This portrays that even at relatively moderate temperatures, higher particle density can trigger the birth of particle clusters, consequently yielding unfavorable strength responses.

In the case of specimen 12/10/700, whose morphology is featured in Fig. 6f, three distinct regions are noticed. The regions are: the dispersed particle region, the segregated particle region, and the clustered particle region. As observed, the dispersed particle region indicates dispersion of particles, whereas the segregated and clustered particles are regions where particles are segregated and agglomeration. The microstructural feature observed is not favorable to strength enhancement as established in the property values. The property values are lower on the basis of the existence of stress concentration and the inducement of residual stress.

The elemental composition analysis of the composites cast at 700 °C is indicated in Table 7, in which major elements are Al (being the matrix), Si, Zn, Mg, Cu, and Mn. The Si content of the base alloy as depicted in Fig. 3 is 0.38%. However, in specimen 3/2/700, the Si amount rose to 0.90%. The Si content increased as the filler count increased. Si content remained nearly constant for specimens 3/10/700, 7.5/6/700, 7.5/6/700, and 12/2/700. Also, there is no appreciable difference in Zn, Mg, Cu, Fe, and Mn based on an insignificant difference in filler count or reinforcement proportion. There was a significant difference in Si content of specimen 12/10/700% at a filler count of 22%, while other elements remained constant. The reinforcement proportion therefore plays a significant role in the elemental composition at various dosages. Figure 9 presents the EDS results of labeled spots in the SEM micrograph displayed in Fig. 8.

Elemental analysis of the spots labeled 1, 2 in Fig. 7a–f reveals the presence of Si and [O] as elements, confirming the presence of silica derived from RHA and GP (Fig. 6a, b). Spots 3 and 4 are spots of agglomeration of particles. Spot EDS results identify major elements as Si, Al, O and others as Mg, Ca, Al, and Na (Table 6). Spots 3, showcased in Fig. 7a–d, are identified as spots of particle agglomerations. Accordingly, the XRD results (Fig. 5a–f) identified no intermetallic phase in the composite, and also spots 3 and 4 are not intermetallic regions rather regions of particle agglomeration.

3.3.3 Composites prepared at 800 ˚C

Specimens prepared at 800 °C are labeled after their composition. Specimens prepared with 3% RHA/6% GP, 12% RHA/6% GP, 7.5% RHA/10% GP, 7.5% RHA/2% GP for experimental runs 9, 5, and 2 are labeled 3/6/800, 12/6/800, 7.5/10/800, 7.5/2/800 in that order, and their respective filler counts are 9.0, 18.0, 17.5 and 9.5%.

The X-ray diffraction pattern for the specimen cast at 800 °C is plotted in Fig. 8. As observed in the plot, identified phases are Al, SiO_2, and phases M_1, M_2, M_3, and M_4. The SiO_2 confirms the existence of the reinforcing additives similar to the pattern displayed by composites prepared at 600 and 700 °C. M_1, M_2, M_3, and M_4 phases detected in the matrices are Mg_2Si, $AlMg(Mn_x)$, and Al(CuMg) (Kim et al. 2019; Sun et al. 2017; Tash and Mahmond 2016) and indicate the presence of intermetallic phases identified as M_1, M_2, M_3, and M_4 in the microstructure shown in Fig. 12.

The morphology of specimen 3/6/800 expressed in Fig. 9a pinpoints the presence of dispersed particles based on particulate dispersion within the melt. Another feature revealed by the microstructure is the presence of micro voids. The findings of Mozammil et al. (Mozammil et al. 2020) and Dhaneswara et al. (Dhaneswara et al. 2019) proved a direct relationship between porosity and temperature. Higher temperature enhances particle dispersion because of high viscosity of the melt, however, the shortcomings include the tendency to entrap air, which is evolved during solidification, resulting in pores. This is a factor responsible for the pores created in the morphology depicted by specimen 3/6/800 (Cao et al. 2019). The morphology of specimen 12/6/800 is highlighted in Fig. 9b. Blow holes are defects associated with high-temperature casting. As a result, absorbed air in liquid metal escapes during solidification from a liquid state. Very high viscosity has the tendency to entrap large volumes of air and, on solidification, the gas is forced to evolve, giving rise to blow holes. Defects generally lead to poor performance of metal. The same is true for the performance of specimen 12/6/800. Figure 9c also featured micro voids for specimen 7.5/10/800, similar to the previously discussed specimen 3/6/800. Another defect in the microstructure represented in Fig. 9d for 7.5/2/800 is the microcrack. A crack may occur as a result of hot tearing.

Elemental analysis of points labeled 1, 2 in the morphological image portrayed in Fig. 9a–d identifies the presence of Si and [O], majorly pinpointing the existence of silica derived from RHA and GP addition. Figure 10a–d depicts elements found in spots M_1, M_2, M_3, and M_4. The major elements existing at these spots are Al, Mg, and Si. The phases identified are Mg_2Si, AlMg(Mnx), AlSi8ZnMg, and Al(CuMg), which confirm the XRD results.

Intermetallic phases in cast metal occur by dint of high-temperature reaction. Diffusion and reaction take place at a faster rate. This sometimes results in the formation of intermetallic compounds, some of which are brittle and do not necessarily improve strength of the composite. These identified spots are stress raisers within the alloy system and are partly responsible for the relatively poor mechanical performance of specimen cast at 800 ˚C as compared with those produced at a relatively moderate 700 °C temperature. In present findings, porosity and intermetallic phases are held responsible for the poorer performance of specimens produced at 800 °C as compared with specimens prepared at 700 °C.

Table 7 Elemental distribution in samples cast at 700 ˚C

Specimen	FC %	Si	Zn	Mg	Cu	Fe	Mn	Other	Al
3/2/700	5	0.90	5.75	1.98	1.54	0.59	0.37	2.11	Balance
3/10/700	13	1.20	5.75	2.38	1.66	0.60	0.22	2.62	Balance
7.5/6/700	13.5	1.24	5.75	3.25	1.67	0.58	0.21	3.21	Balance
7.5/6/700	13.5	1.26	5.73	3.36	1.68	0.61	0.27	3.08	Balance
12/2/700	14	1.25	5.70	3.10	1.68	0.59	0.23	3.33	Balance
12/10/700	22	3.12	5.61	3.41	1.80	0.58	0.27	3.42	Balance

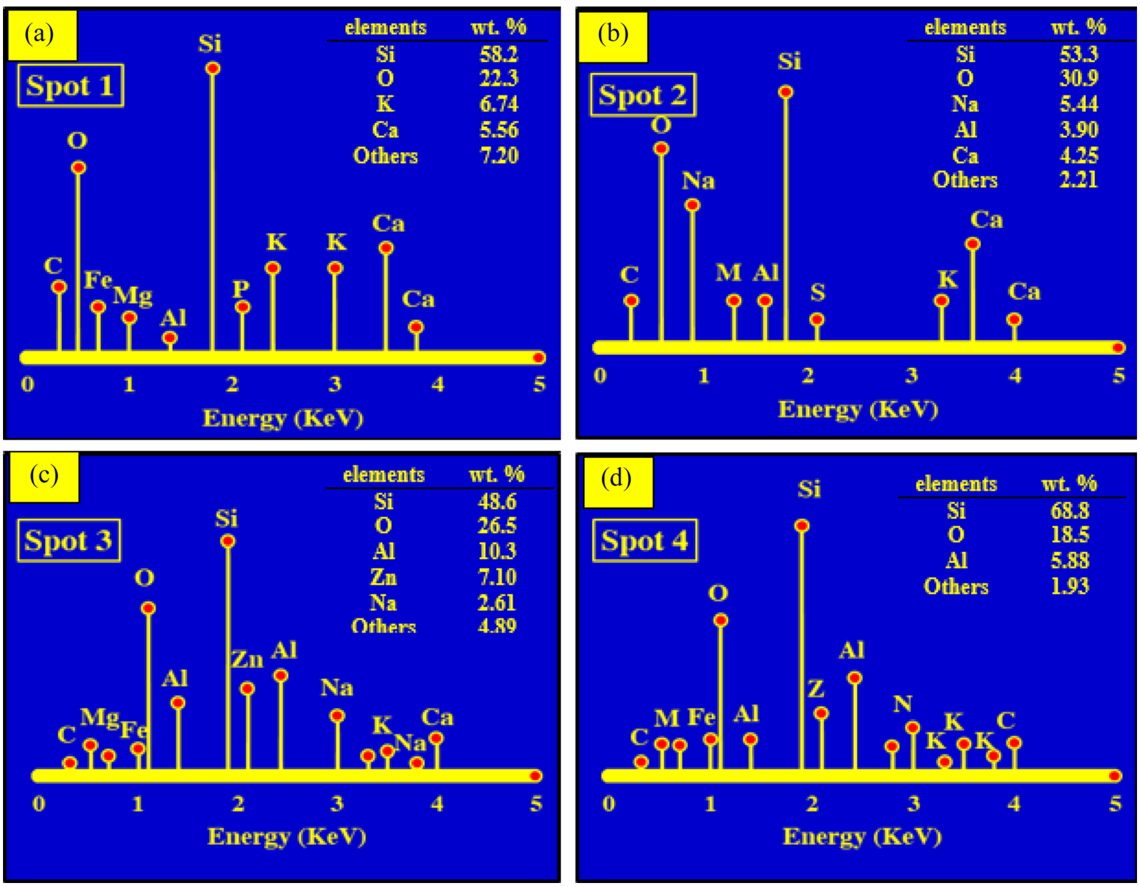

Fig. 7 Spot EDS elemental results on specimen cast at 600 ˚C prepared with (**a**) 3% RHA/6% GP (**b**) 7.5% RHA/2% GP (**c**) 7.5% RHA/10% GP and (**d**) 12% RHA/6% GP

The elemental composition analysis of the composites stirred at 800 ˚C is indicated in Table 7, in which major elements are Al (being the matrix), Si, Zn, Mg, Cu, and Mn. The Si content of the base alloy as depicted in Fig. 1 is 0.38%. However, in specimen 3/6/800, the Si amount rose to 1.14% at a filler count of 9%. with an increasing particulate count of 18 and 17.5% for specimens 12/6/800 and 7.5/10/800, respectively. The Si content showed no significant difference between specimens 12/6/800 (prepared at 800 ˚C) and 12/6/600 (prepared at 600 ˚C). Equally, the particulate count is 18%. The morphology revealed various features, including agglomerations in specimen 12/6/600 and blow holes and intermetallic phases of Mg2Si; AlMg(Mn_x) in specimen 12/6/800. Disparity in the features observed in the microstructures is based on temperature effects. Similarly, the microstructure of specimen 7.5/10/800 (prepared at 800 °C) contained phases of Mg2Si, AlMg(Mn_x), and $AlSi_8ZnMg$, in contrast to the microstructure of specimen 7.5/10/600 (prepared at 600 °C), which contained particle clusters.

The difference in elemental proportion between specimen 3/6/800 and specimen 7.5/2/800 is insignificant, and

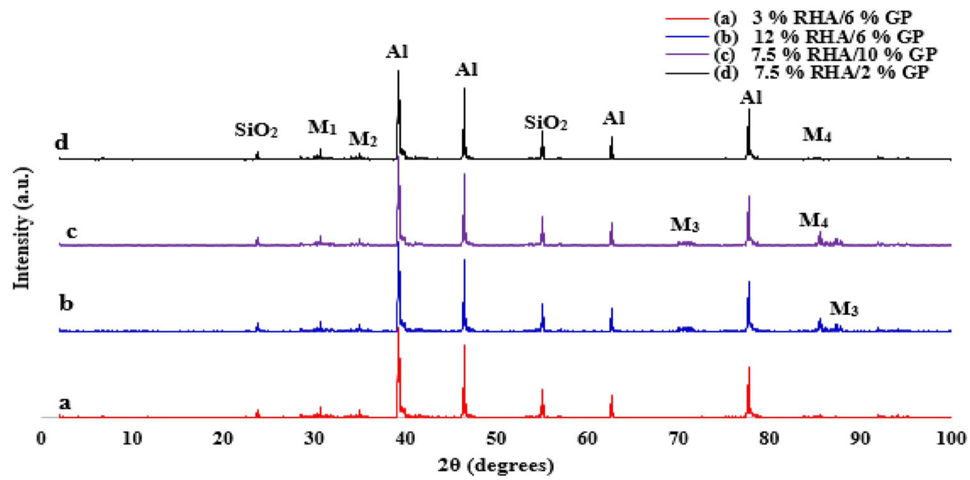

Fig. 8 X-ray diffraction patterns for composites cast at 800 ˚C prepared with (**a**) 3% RHA/6% GP (**b**) 7.5% RHA/2% GP (**c**) 7.5% RHA/10% GP (**d**) 12% RHA/6% GP

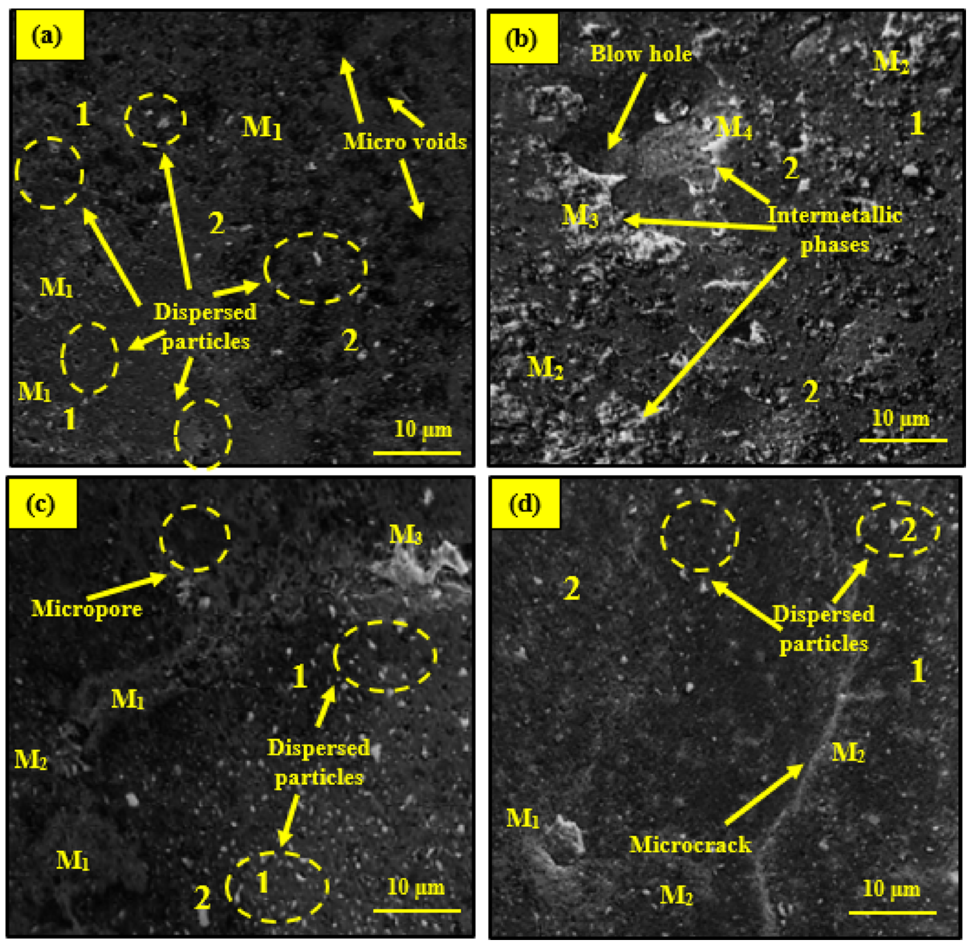

Fig. 9 FESEM morphological image of specimen cast at 800 ˚C and prepared with (**a**) 3% RHA, 6% GP (**b**) 12% RHA, 6% GP (**c**) 7.5% RHA, 10% GP and (**d**) 7.5% RHA, 2% GP

intermetallic phases are Mg_2Si; $AlMg(Mn_x)$ dominant, as observed in the microstructure and confirmed by XRD results, owing to the high diffusibility of atoms at high temperatures. In the case of specimen 12/6/800 and specimen 7.5/10/800 with filler counts of 18 and 17.5%, respectively, there is a consequential difference in Mg and Cu elements, an observation held responsible for the formation of the Al(CuMg) phase in specimen 7.5/10/800. This report showed the role of stirring temperature and filler counts on the morphological features, phase changes, and intermetallic formation.

Peak values for all properties are attained at the blend of 7.5% RHA and 6% GP, except for hardness. A maximum

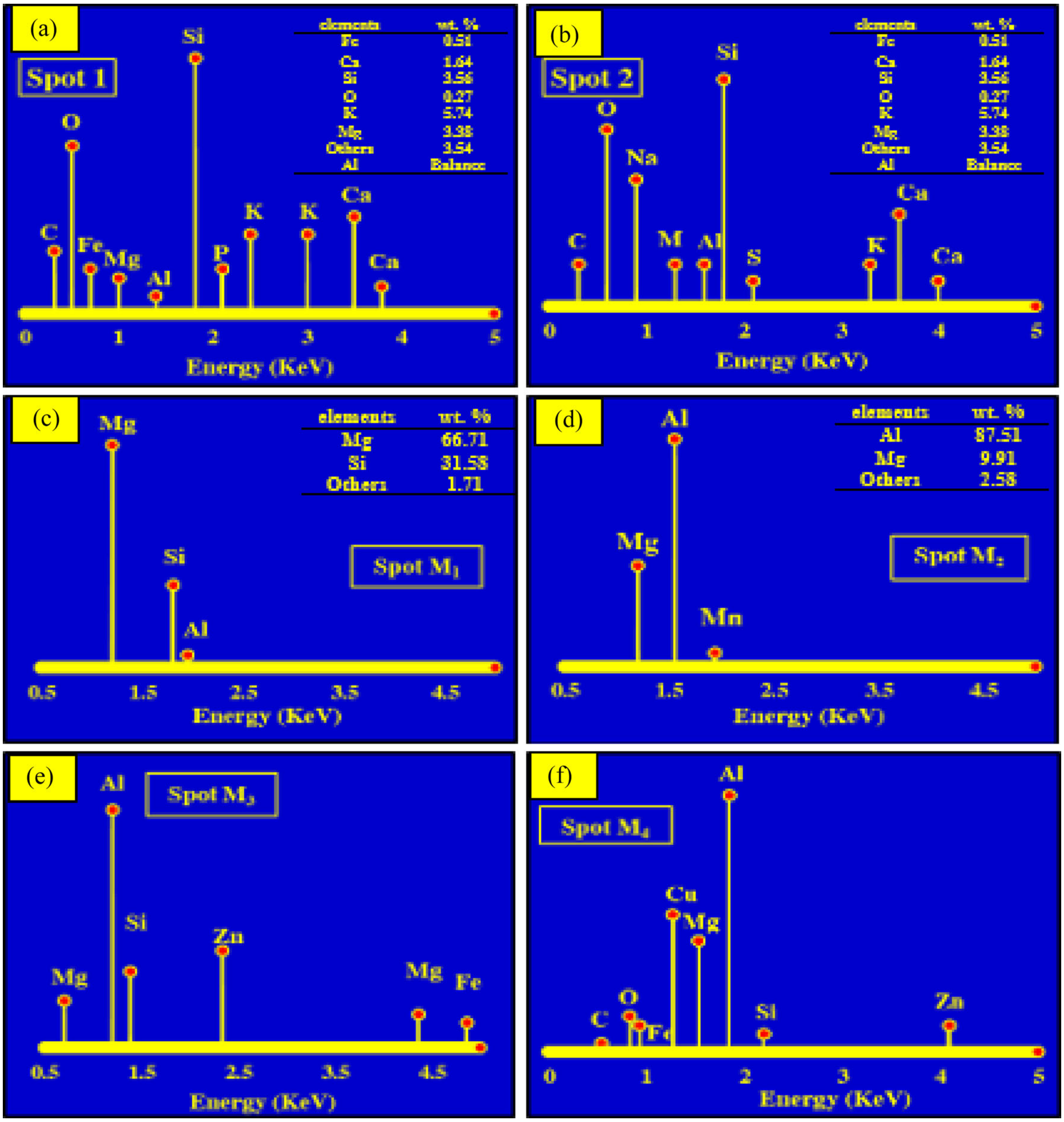

Fig. 10 Spot EDS elemental results on specimen cast at 800 ˚C prepared with (**a**) 3% RHA/6% GP (**b**) 7.5% RHA/2% GP (**c**) 7.5% RHA/10% GP (**d**) 12% RHA/6% GP

hardness value of 3/10/700 was realized; a marginal difference of 3.95% over that of specimen 7.5/6/700. Discrepancy can occur by reason of higher GP content. However, the difference can be ignored since it is marginal. This result therefore establishes 700 °C as an adequate casting temperature for the composite developed.

3.4 Statistical analysis of experimental outcome

Obtained experimental results were subjected to analysis of variance (ANOVA), mathematical modeling, model validation, response surface analysis and optimization.

3.4.1 Analysis of variance (ANOVA)

Analyses of variance were conducted to estimate if the differences obtained for the data are statistically significant. The evaluation was done at a 95% confidence level and a 5% significance level. A probability (p) value was chosen as the basis for determining the significance of a given parameter or interaction. A p-value less than 0.05 indicates a significant contribution. By contrast, when the value is greater than 0.05, the contribution is insignificant (Table 8).

Table 9 highlights the ANOVA results on the responses. The p-value for the models of the responses is < 0.05, indicating that the models are fit to represent the data. The residual

Table 8 Elemental distribution in samples cast at 800 °C

Specimen	FC %	Si	Zn	Mg	Cu	Fe	Mn	Other	Al
3/6/800	9	1.14	5.74	2.40	1.63	0.54	0.27	2.22	Balance
12/6/800	18	2.11	5.75	2.44	1.68	0.58	0.31	2.84	Balance
7.5/10/800	17.5	2.39	5.73	3.28	1.76	0.51	0.28	3.52	Balance
7.5/2/800	9.5	1.19	5.68	2.41	1.65	0.53	0.29	2.67	Balance

FC is filler count %

Table 9 ANOVA on responses

Source	TS	UTS	FS	HD	IS	CS
Model	< 0.0001	< 0.0001	< 0.0001	< 0.0001	< 0.0001	< 0.0001
A-RHA	< 0.0001	0.0005	0.0841	< 0.0001	< 0.0001	< 0.0001
B-GP	0.0012	0.0033	0.0009	< 0.0001	0.0003	< 0.0001
C-Temperature	0.0002	0.0026	0.0034	< 0.0001	< 0.0001	< 0.0001
AB	0.0328	0.0588	0.0238	0.3348	0.9820	0.8325
AC	0.9388	0.0933	0.9337	0.7759	0.0229	0.1682
BC	0.7983	0.7315	0.9779	0.0093	0.9281	0.2665
A^2	< 0.0001	< 0.0001	< 0.0001	0.9184	< 0.0001	< 0.0001
B^2	< 0.0001	< 0.0001	< 0.0001	0.0833	< 0.0001	0.1722
C^2	< 0.0001	< 0.0001	< 0.0001	< 0.0001	< 0.0001	< 0.0001
Lack of Fit	0.7900	0.8500	0.4000	0.6853	0.1615	0.7058
R^2	0.9905	0.9875	0.9846	0.9898	0.9920	0.9795
Adjusted R^2	0.9783	0.9713	0.9648	0.9768	0.9818	0.9888
Predicted R^2	0.9571	0.8042	0.8569	0.9424	0.9560	0.9771
Adeq. Prec	26.33	22.00	18.60	30.14	26.77	24.56

coefficient of correlation ($R^2 = 0.9905$) for the models is respectively > 0.95, confirming a high correlation between the models and the respective data. The models are therefore > 95% dependable to represent the data with < 5% variability. Furthermore, the p-values for the lack of fit are > 0.05. Therefore, the models present a high degree of fitness with the residuals. The difference between adjusted R^2 and predicted R^2 is less than 0.2 (20%), further pointing to a statistically fit model. The value of Adeq. precision for the responses is > 4, affirming the models can be used to traverse the design space.

Table 9 shows that factor A (RHA) has a significant influence on the responses TS, UTS, HD, IS, and CS ($p < 0.05$), but only a marginal influence on FS ($p > 0.05$). Regarding all properties, the p-value of factors B (RHA) and C (temperature) is < 0.05. By inference, the contributions of RHA and temperature to all responses are consequential. *P*-values for cross interactions between the factors (AB, AC, BC) are > 0.05 for all properties, implicating that the contributions of the cross interactions on the responses are inconsequential. Relating to the properties, square interaction A^2 had a significant effect on all responses except microhardness. Meanwhile, B^2 demonstrated significant influence on all the responses, with the exception of microhardness and compressive strength. The contribution of interaction C^2 is shown to be substantial on all responses (p-value < 0.05).

3.4.2 Mathematical models

Equations 2–7 are the mathematical models for yield strength, ultimate tensile strength, microhardness, flexural strength, impact strength and compressive strength respectively. From the models, the coefficients of factors A and C are positive. This means that the terms have a resultant positive (synergetic) effect on the responses. Factor B possesses a positive coefficient except in the case of microhardness, which means factor B is antagonistic to microhardness. Square interaction A^2 showed a resultant negative influence on YS, UTS, FS, IS, and CS but a resultant positive contribution on HD. From the models, it is deduced that the contributions of B^2 and C^2 are antagonistic to all responses. In the case of the cross interactions, AB is synergetic to FS, IS, and CS but antagonistic to YS, UTS, and HD. Relating to interaction AC, the contribution is synergetic pertaining to YS and CS, but antagonistic to UTS, HD, FS, and IS. Factor BC manifested a resultant positive influence on YS, UTS, and HD but a resultant negative contribution on FS, IS, and CS.

$$\begin{aligned}YS = & -4100.3063 + 98.4722\,A + 85.3604\,B \\ & + 12.3758\,C - 1.3889\,AB + 0.0017\,AC \\ & + 0.0063\,BC - 6.9963\,A^2 - 7.3391\,B^2 - 0.0092\,C^2\end{aligned} \quad (2)$$

$$\begin{aligned}UTS = & -6114.3833 + 158.7500\,A + 88.1271\,B \\ & + 17.5603\,C - 1.4028\,AB - 0.0483\,AC \\ & + 0.0100\,BC - 8.4741\,A^2 - 7.7719\,B^2 - 0.0126\,C^2\end{aligned} \quad (3)$$

$$\begin{aligned}HD = & -703.3326 + 3.7037\,A - 1.4333\,B \\ & + 2.2863\,C - 0.0972\,AB - 0.0011\,AC \\ & + 0.0150\,BC + 0.0086\,A^2 - 0.2078\,B^2 - 0.0016\,C^2\end{aligned} \quad (4)$$

$$\begin{aligned}FS = & -3856.2750 + 58.0833\,A + 56.9646\,B \\ & + 11.9008\,C + 1.3889\,AB - 0.0017\,AC \\ & - 0.0006\,BC - 4.2000\,A^2 - 6.2844\,B^2 - 0.0087\,C^2\end{aligned} \quad (5)$$

$$\begin{aligned}IS = & -33.5943 + 0.5969\,A + 1.0940\,B + 0.1127\,C \\ & + 0.0001\,AB + 0.0007\,AC - 0.0000\,BC - 0.0814\,A^2 \\ & - 0.1002\,B^2 - 0.0001\,C^2\end{aligned} \quad (6)$$

$$\begin{aligned}CS = & -7131.0729 + 94.2222\,A + 31.7292\,B + 21.0042\,C \\ & + 0.0278\,AB + 0.0078\,AC - 0.0069\,BC - 6.2778\,A^2 \\ & - 0.2109\,B^2 - 0.0153\,C^2\end{aligned} \quad (7)$$

3.5 Response surface analysis and contour plots

3.5.1 Yield tensile strength

Figure 11a showcases the response plot of the interaction between RHA and GP and the effect of such interaction on yield strength response when temperature is held at 700 ˚C. Proportion of 3–7.5 wt. % RHA and 2–6 wt. % GP led to strength enhancement. The outcome revealed in this study between 3 and 7.5 wt. % RHA is similar to the findings of Ahamed et al. (Ahamed et al. 2016) in which progressive enhancement of tensile strength was observed with 3–9% of RHA. Likewise, Adediran et al. (ASTM E 9–09 2018) reported increment in tensile strength when glass particulate was introduced into Al 6061 melt in similitude with findings showcased between 2 and 6% GP in this study. The boost in strengths is attributed to coexistence between the two forms of particulate and good adhesion with the matrix based on particle strengthening mechanism. In the investigation carried out by Adekomaya and Adamu (Ademokoya and Adama 2017), inclusion of reinforcement particles resulted in progressive enhancement of strength. It was however noted that 7.5–12 wt. % dosage of RHA combining with 6–10 wt. % GP ensured reduction in response. Reason for the reduction in strength is associated with high density of the particles ensuing clustering of particles within the matrix as reported by Roether and Boccaccini (Roether and Boccaccini 2005). Virkunwar et al. (Virkunwar et al. 2018) associated the findings to poor wettability existing between particulates; and they observe decrease in tensile strength when RHA was beyond 8% in their study. As observed in Fig. 13a, the point of intersection for the inflexions 7.5% RHA and 6% GP corresponds to strength value of 603 MPa (a 38.9% over the value of the reference mix). The two factors A and B demonstrated inverted parabolic interaction profile. The general profile for the combined interaction is a domed-shaped profile. Contour plots show different regions where varying property response can be obtained at different intervals of the experimental inputs. Important region is the optimal region which give range of values for optimal response. Figure 11b shows the contour plot of the interaction. Optimum zone is indicated as point A for values > 600 MPa obtainable when 4.8–8.3 wt. % RHA is combined with 4.1–6.8 wt. % GP when maintaining temperature at 700 ˚C. Hence, at constant 700 ˚C, optimum yield strength can be obtained by blending 4.8–8.3 wt. % RHA with 4.1–6.8 wt. % GP.

Similarly, as in the case of interaction RHA versus temperature, as it affects the response, holding GP constant at 6 wt. % (Fig. 11c), 3–7.5 wt.% RHA at temperatures of 600–700 ˚C engendered strength improvement. Moderate temperature ensues moderate viscosity permitting even dispersion of the particles effecting better performance in the material (Shin et al. 2021). Proportions of 7.5–12% RHA at temperature range of 700–800 ˚C amounted to decrease in strength. Higher casting temperature has tendency to initiate higher chemical reaction amounting to formation of some intermetallic compounds capable of deteriorating the strength of the alloy (Barbosa et al. 2014). The two parameters displayed inverted parabolic interaction profile and intersection point of inflexion was reached at coded level 0 (6 wt. % graphite and 700 ˚C) corresponding to 605.9 MPa. General profile for the interaction is taken to be domed shape. From the contour plot of the interaction displayed in Fig. 11d, input of 4.6–8.5 wt. % RHA infused into Al 7075 melt at temperature range of 625–725 ˚C will achieve optimum result of yield strength > 600 MPa, when holding GP constant at 6 wt. % (Fig. 12).

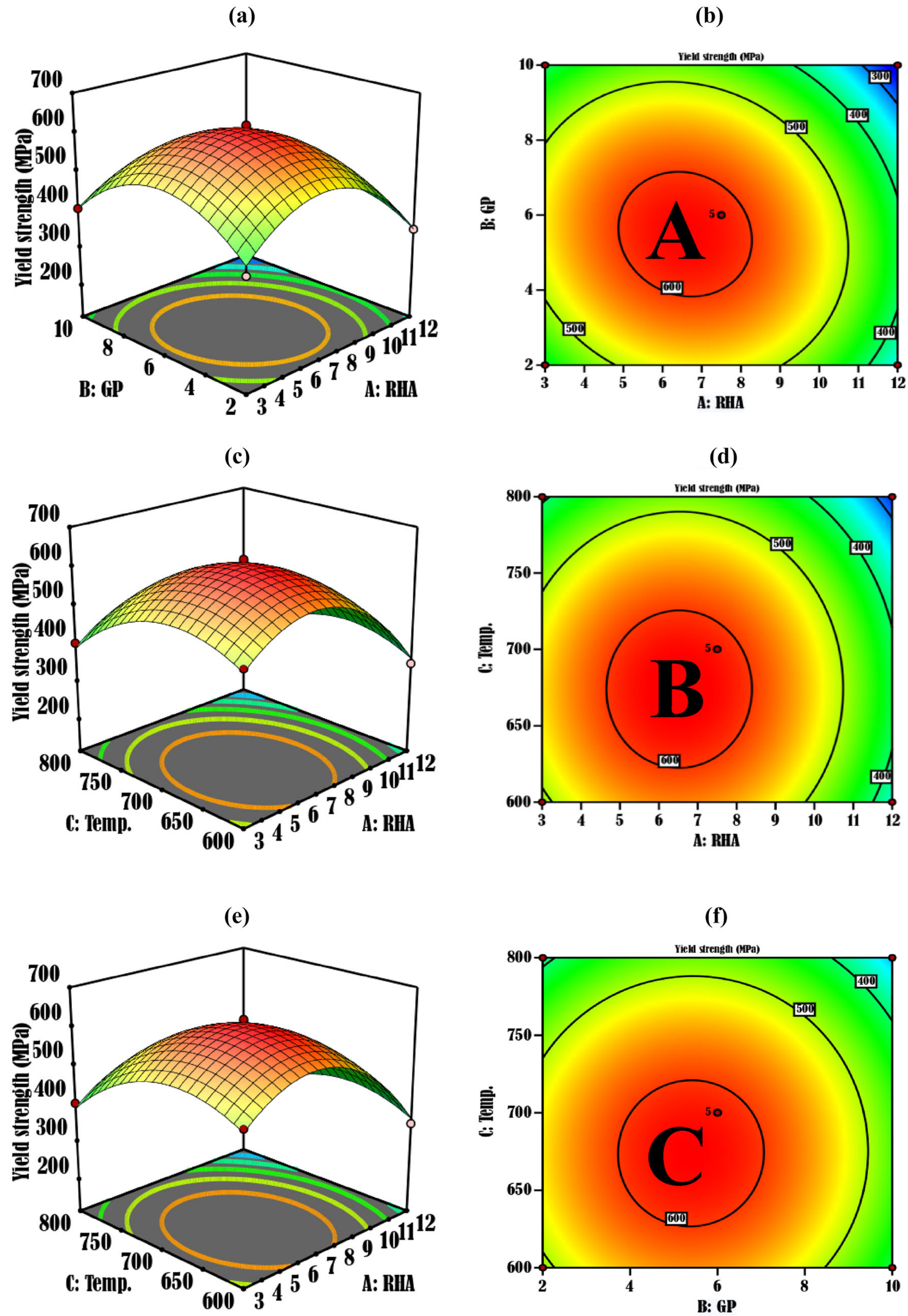

Fig. 11 Response surface and contour plots revealing effects of interactions on yield strength as represented by interactions (**a**, **b**) rice husk ash vs glass powder (**c**, **d**) rice husk ash vs temperature (**e**, **f**) glass powder vs temperature

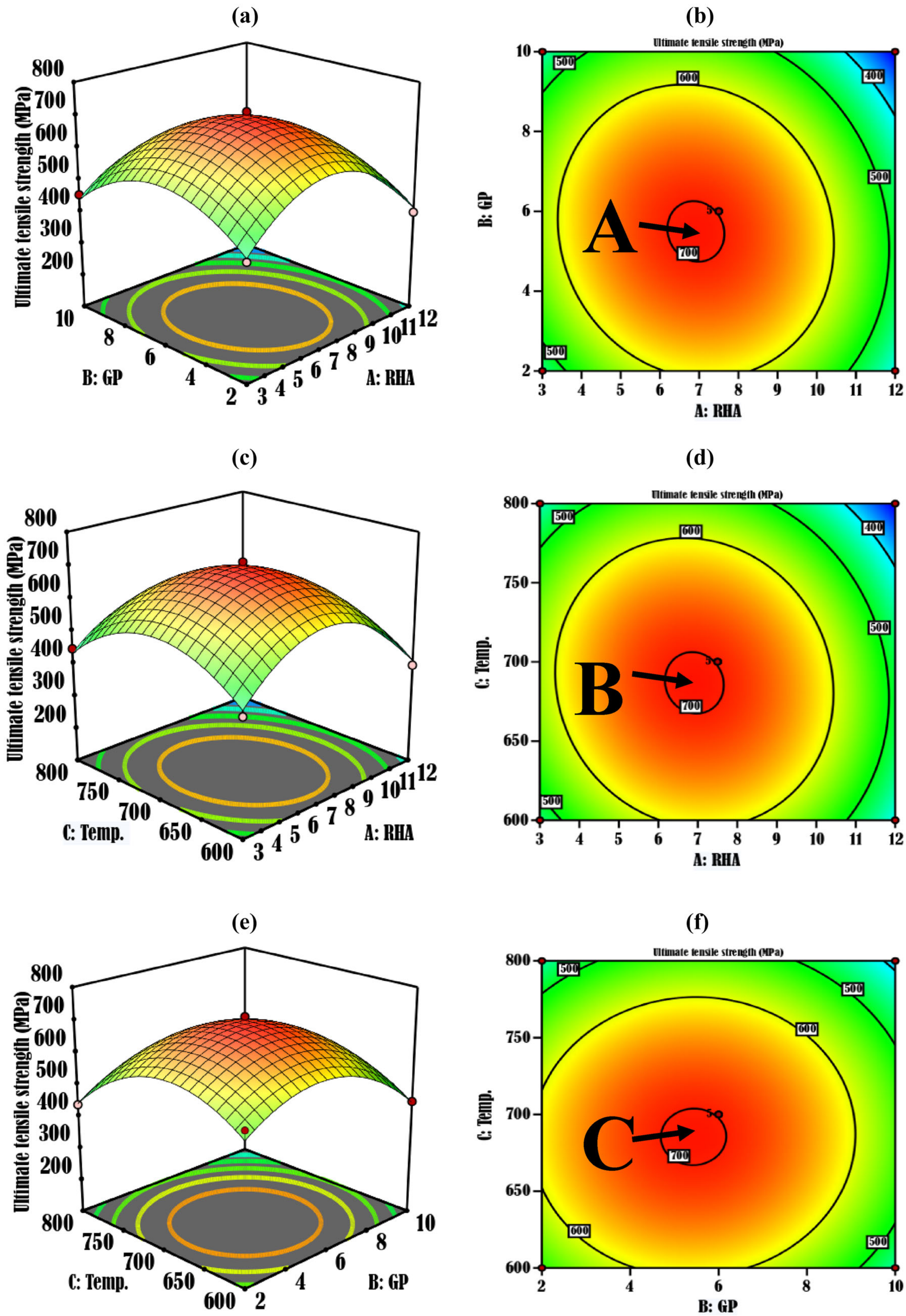

Fig. 12 Response surface and contour plots revealing effects of interactions on ultimate tensile strength as represented by interactions (**a**, **b**) RHA vs GP (**c**, **d**) RHA vs temperature (**e**, **f**) GP vs temperature

Interaction GP versus temperature is demonstrated in Fig. 11e at constant RHA of 7.5 wt. %. GP proportion of 2–6 wt. % infused into the composite at temperatures between 600 and 700 ˚C led to enhancement of strength. Madhankumar et al. (Madhankumar et al. 2018) revealed that glass powder possesses good cohesion with other particulates like SiC toward enhancement of the tensile strength of aluminum composite. Meanwhile, 6–10 wt. % GP at 700–800 ˚C ensued strength reduction. The depreciation in strength is hinged on high particle density within the matrix engendering particle clustering (Swamy et al. 2011; Anyalem 2020b). The two factors exhibited inverted parabolic profile yielding combined domed-shaped profile. The intersecting inflexion point was detected at coordinates 6 wt. % GP and 700 ˚C corresponding to 597.6 MPa. As observed in the contour plot of Fig. 11f, optimal zone is indicated as C. Yield strength > 600 MPa can be obtained when 3.8–7.1% of GP is blended with 7.5 wt. % constant dosage of RHA at temperature range of 625–720 ˚C.

3.5.2 Ultimate tensile strength

The response plot of the interaction RHA versus GP and the outcome of the interaction on ultimate strength response holding temperature at 700 °C is illustrated in Fig. 12a. Particulate loading of 3–7.5 wt. % RHA and 2–6 wt. % GP prompted strength enhancement. This accretion in strength occurs on account of the uniform distribution of both particles within the composite, ensuing strong bonds, consequently effecting a boost in UTS. Moreso, reduction in particle distance by virtue of particulate presence encourages impediment to dislocation movement in the matrix. Further additions of 8 and 10 wt.% GP amounted to a reduction occasioned by increased particle density. Combined particulate addition in aluminum alloy has been studied and reported to improve the tensile properties of hybrid aluminum composites (Myalska-Glowacka et al. 2022; Khan et al. 2015; Venkatesh et al. 2019). These studies achieved enhancement of ultimate tensile strength of Al 6061 when rice husk ash was introduced into the melt from 2 to 8 wt.% agreeing with the findings depicted in this study. From the surface plot (Fig. 14a), 7.5–12 wt. % dosage of RHA interplaying with 6–10 wt. % GP particles provoked a decrease in response owing to particulate coarsening. An investigation carried out by Usman et al. 2014a revealed the effect of rice husk ash (RHA) addition on the ultimate tensile strength of the aluminum composite. 5%–10% RHA in the matrix expedited a boost in value, and beyond 10%, there was a depreciation in strength. Equally, Adediran et al. (ASTM E 9–09 2018) improved the ultimate tensile strength of aluminum matrix with glass powder up to 6%, beyond which there was strength reduction. Akinwande et al. (Akinwande et al. 2022d) combined RHA and GP in recycled melt and observed that the blend of 9% RHA and 4% GP begat optimum improvement (an improvement of 52.81% over the reference mix) in tensile strength, showing that the combination of the two additives contributes to strength enhancement in aluminum matrix. The point of inflexion corresponding to a strength response of 704.4 MPa was achieved at corresponding values of 7.5 wt. % RHA and 6 wt. % GP. The two factors, A and B, manifested an inverted parabolic interaction profile, portraying a combined domed-shaped profile. In Fig. 12b, region A is the optimum zone as regards the interaction between RHA and GP. At a constant temperature of 700 °C, a feasible RHA dosage of 6.6–7.8 wt.% and GP loading of 4.8–6.2 wt.% at a constant temperature of 700 °C.

In terms of the interaction RHA versus temperature, as it affects the ultimate tensile strength response at a constant GP of 6 wt.% (Fig. 12c), 3–7.5 wt.% RHA at temperatures of 600–700 °C resulted in an improvement, whereas particulate loading of 7.5–12% RHA used at 600–700 °C ensued in a decrease in strength. A similar study revealed how rice husk ash combined with fly ash yielded optimum tensile performance at 6% (Subrahmanyam et al. 2016). The viscosity of a metal melt is dependent on casting temperature and it influences the properties of the developed composite (Ferreira et al. 2019). At lower viscosity, the reinforcing particles have lower mobility within the melt, causing segregation, agglomeration, and clustering. If the viscosity is high due to high temperature, particles possess a high amount of kinetic energy with the possibility of even dispersion. At much higher temperatures, there is a tendency for gas entrapment. However, determining the moderate casting temperature for even casting is not easy. In this study, temperatures between 600 and 700 ˚C seem moderate, beyond which there is strength reduction. The two parameters RHA and temperature displayed an inverted parabolic interaction profile and the intersecting point of inflexion was reached at a coordinate of 6 wt. % graphite and 700 °C, corresponding to 704.7 MPa. The general profile for the interaction is a domed shape profile. From the contour plot of the interaction displayed in Fig. 12d, an input of 6.20–7.6% RHA at 675–715 °C will achieve an optimum result of strength > 700 MPa, holding GP constant at 6 wt.%.

Figure 12e depicts the GP versus temperature interaction at a constant RHA of 7.5 wt.%. A GP proportion of 2–6 wt.% included at temperatures of 600 and 700 °C resulted in strength improvement, whereas a GP proportion of 6–10 wt.% added at temperatures of 700–800 °C engendered strength reduction. A comparable outcome was showcased by Mathur and Barnawal (Mathur and Barnawal 2013) in which temperatures between 700 and 725 °C were favorable to the UTS performance of Al-4Cu, beyond which an increase in temperature became detrimental to the strength value. The two factors RHA and GP depicted an inverted parabolic profile, yielding a combined domed-shaped profile.

The intersecting inflexion point was pinpointed at coordinates 6 wt. % GP and 700 °C, corresponding to 704.3 MPa. As observed in the contour plot of Fig. 12f, the optimal zone is indicated as C. When 4.4–6.3 wt.% GP is used at temperatures ranging from 665 to 720 °C and RHA is kept at 7.5 wt.%, 700 MPa can be achieved.

3.5.3 Flexural strength

Figure 13a reflects the surface plot of the interaction between RHA and GP and the effect on flexural strength response at a constant temperature of 700 °C. Interplay between 3 and 7.5 wt. RHA and 2–6 wt. % GP led to enhancement of strength. The feat is attributable to improved interparticle cohesion between the particles owing to favorable interaction between them. Nevertheless, the combination of 7.5–12 wt. % RHA and 6–10 wt. % GP aroused strength reduction. The depreciation in strength is traceable to micro voids and the presence of secondary (intermetallic) phases is antagonistic to strength improvement and ductility. There are scarce studies focused on the flexural strength of aluminum matrix using glass powder and rice husk reinforcement. Even though there are similar studies involving other ceramic particulates. The outcome of the studies of Das et al. (Das et al. 2019) revealed that SiC particulate plays a significant role in enhancing the flexural strength of Al 7075. A hybrid aluminum composite developed by Saravanakumar and Sasikuma (Saravanakumar and Sasikumar 2018) involved the blend of alumina and graphite into the melt. Optimum flexural strength was attained by the blend of 6% alumina and 1% graphite was infused. Akinwande et al. (Akinwande et al. 2022d) showed that the combination of RHA and GP has a significant effect on the flexural properties of aluminum matrix. The two factors RHA and GP displayed an inverted parabolic interaction profile, effectuating a combined domed shape interaction profile. When the temperature is held constant at 700 °C, the intersection points for the two factors occur when RHA proportion is 7.5 wt.% and GP proportion is 6 wt.%, totaling 554.5 MPa. As observed in the optimum zone A of the contour plot for the interaction in Fig. 13b, input of 6.2–7.8 RHA combined with 4.6–5.7 wt.% GP will achieve an optimum result of flexural strength > 550 MPa, holding temperature constant at 700 °C.

Figure 13c highlights the surface plot of the interaction between factors A and C and the effect on flexural strength, holding GP constant at 6 wt. %. Strength increases when 3–7.5% RHA is infused in the melt at temperatures ranging from 600 to 700 °C. The observation is linked to enhanced closed packing in the matrix, amounting to a lowering of plastic deformation during loading. Even so, the proportion of 7.5–12 wt. % RHA addition at a temperature range of 700–800 °C culminates in strength reduction. Observed depreciation in strength occurs on account of particle agglomeration and intermetallic phases present due to high-temperature reactions. The interaction profile for each factor RHA and temperature is parabolic, resulting in a combined profile of a dome shape. The curvature point exists at coordinates of 7.5 wt. % RHA and 6 wt. % GP, yielding a value of 552.5 MPa. In Fig. 13d, region B is the optimum zone as regards the interaction between RHA and GP. At a constant GP of 6 wt.% and an RHA dosage of 6.3–7.9 wt.%, and a stirring temperature of 670–690 °C.

The surface plot for the effect of the interaction GP versus temperature when RHA is held constant at 7.5 wt.% is shown in Fig. 13e. Employing 2–6 wt.% GP at temperatures of 600 and 700 °C resulted in strength improvement, whereas employing 6–10 wt.% GP at temperatures of 700–800 °C resulted in strength reduction. The interaction profile for each parameter is parabolic and domed-shaped for the combined. The turning point exists at a coordinate of 6 wt. % GP and 700 °C, yielding a yield strength value of 554.5 MPa. As identified in the contour plot of Fig. 13f, the optimal region is indicated as C. Between temperatures of 640–710 °C, 4.6–6.4% of GP is incorporated, with RHA remaining at 7.5 wt.%.

3.5.4 Microhardness

A response surface plot for the interaction RHA versus GP at a constant temperature of 600 °C is presented in Fig. 14a. Admixture of 3–12 wt. with 2–10 wt. % GP contributes significantly to the enhancement of hardness. Mishra et al. (Selvam et al. 2021) revealed the significance of RHA in the improvement of the hardness of aluminum alloy composites. Verma and Vettivel (Verma and Vettivel 2018) carried out response surface optimization of Al 7075 reinforced with RHA and B_4C. Interaction between 1 and 5% RHA and 1–5% B_4C enkindled progressive improvement in microhardness. The surface plot of the interaction between RHA and B_4C in the study is in sync with the result of the surface plot depicted for the interaction between GP and RHA in the present study. The accretion in hardness associated with an increment in particulate presence is associated with the hardness of the particulates and the closed-packed structure exhibited at the surface. The two input factors, RHA and GP, manifested a positive linear interaction plot, giving rise to a gable-shaped interaction profile. Maximum hardness for the interaction occurred when 12 wt. % RHA and 10 wt. % GP were blended into the melt at 700 °C, correlating with a 204 Hv value for hardness. In Fig. 14b, the optimum zone is indicated as point A for values > 200 HV is realizable on a combination of RHA within the range of 9.7–12 wt.% and GP in the range of 8.5–10 wt.%.

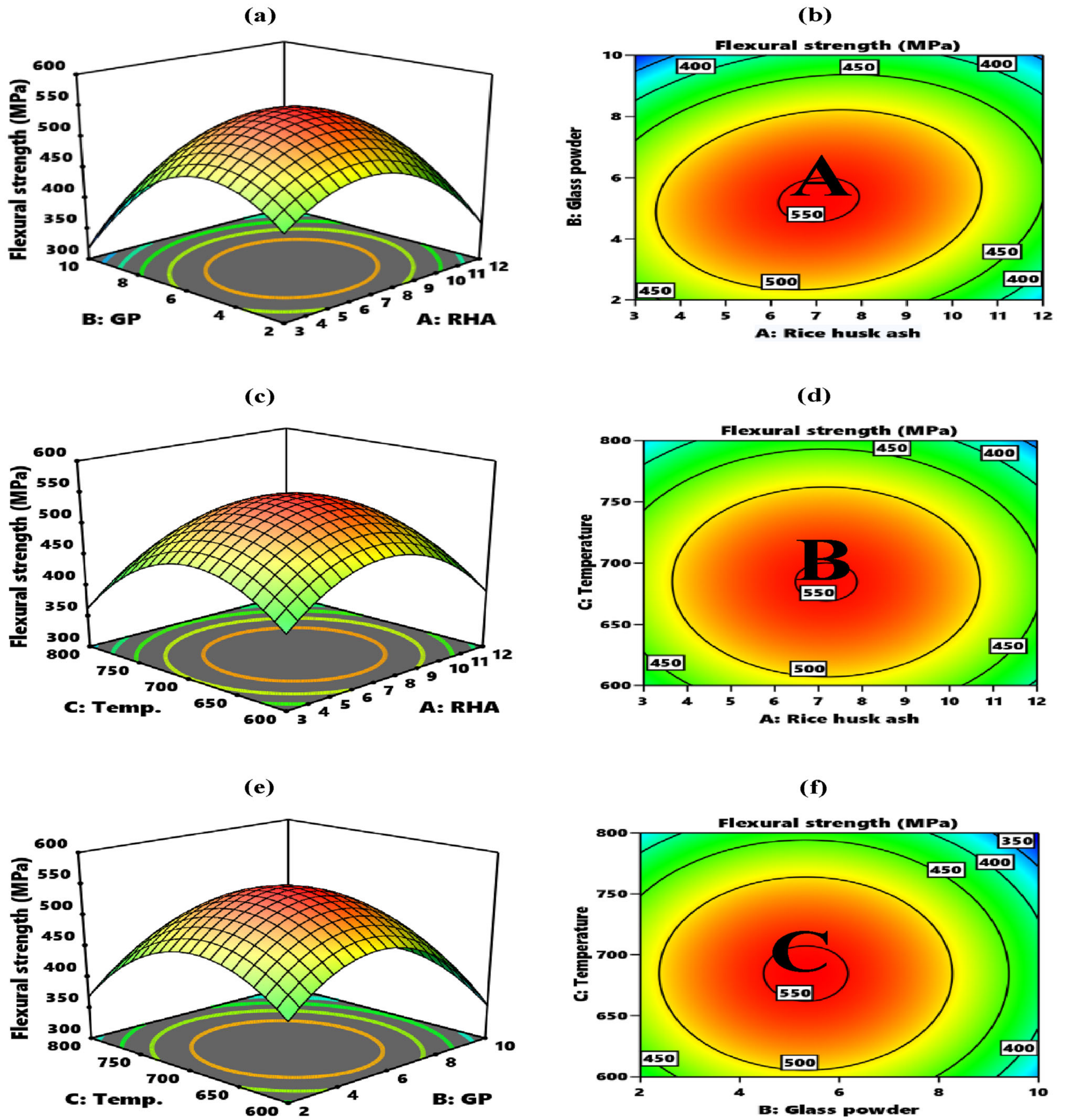

Fig. 13 Response surface and contour plots revealing effects of interactions on flexural strength as represented by interactions (**a**, **b**) RHA vs GP (**c**, **d**) RHA vs temperature (**e**, **f**) GP vs temperature

Figure 14c epitomizes the surface plot of the interaction between factors RHA and temperature with respect to hardness at a constant GP proportion of 6 wt.%. Even though the temperature range of 600 and 700 °C is favorable to hardness, 3–12 wt.% RHA resulted in an improvement in hardness. Udoye et al. (Myalska-Glowacka et al. 2022) achieved optimal microhardness by infusing Al 6061 with 8% RHA. The trend in their study aligns with the trend presented by RHA in this study with regards to microhardness. However, 700–800 °C begat a slight decrease in hardness. According to Mathur and Barnawal (Mathur and Barnawal 2013), temperatures between 700 and 725 °C were favorable to hardness, while temperatures between 725 and 750 °C caused a decrease in hardness value due to the presence of defects such

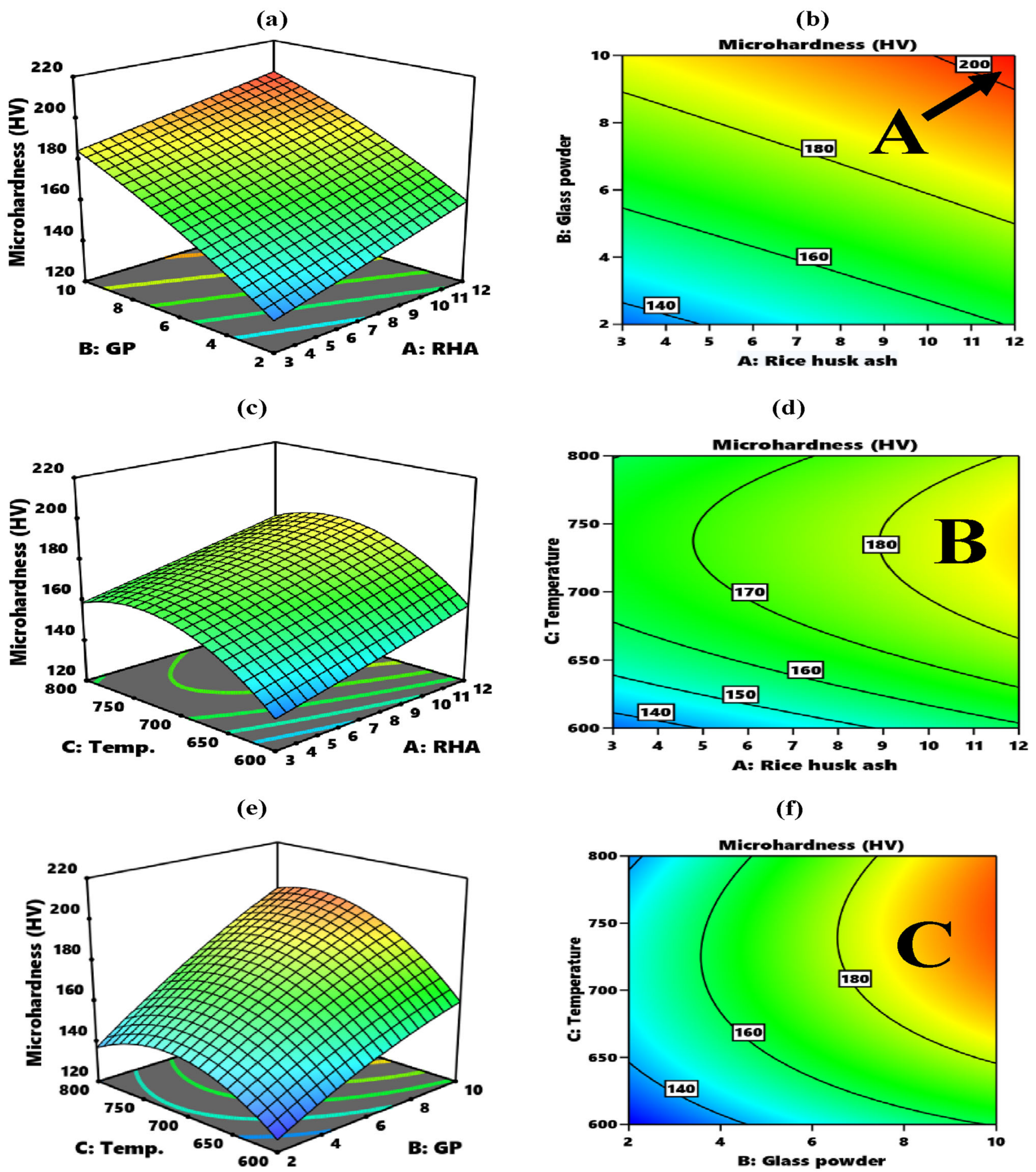

Fig. 14 Response surface and contour plots revealing effects of interactions on microhardness as represented by interactions (**a**, **b**) RHA vs GP (**c**, **d**) RHA vs temperature (**e**, **f**) GP vs temperature

as micro cracks, surface micro-porosity, and weakened bonds at the surface. All this elicits a weakening of surface hardness. While RHA exemplifies a positive linear profile, temperature reflects a half-parabolic interaction profile, yielding a combined half-barrel shaped interaction profile. Maximum hardness was attained when 12% RHA was blended with 6% GP at 700 °C, corresponding to 187 HV. From the contour plot of the interaction presented in Fig. 14d, an input of 9.2–12 wt.% RHA at a temperature of 620–800 °C will achieve an optimum hardness value > 180 MPa HV, holding GP constant at 6 wt.%.

Figure 14e illustrates the surface plot for the influence of the interaction "GP versus temperature" on microhardness when holding RHA at 7.5 wt.%. Usage of 2–10 wt. % GP resulted in an increment in hardness. Adediran et al. (ASTM E 9–09 2018) validate the use of GP in this study as similar accretion in hardness with progressive assimilation of GP was reported. The temperature range of 600 and 700 °C favors enhancement of hardness, while the temperature range of 700–800 °C is detrimental to hardness. Therefore, the moderate peak temperature for optimum hardness for the interaction is 700 °C. Klemens et al. (Klemens et al. 2019) obtained a maximum casting temperature of 750 °C for aluminum 7075 alloy. The interaction profile for glass powder parameters was slimily positive linear, while temperature displayed a half-parabolic profile. Hence, the interplay between GP and temperature as it affects micro hardness is said to be inverse when temperature exceeds 700 °C, yielding a combined half-barreled shape interaction profile with a steeper slope as compared with the combined shape obtained for the interaction RHA vs temperature. This implies that for the interaction GP vs temperature at 7.5% RHA (constant dose), temperature beyond 700 °C is more detrimental to hardness as compared with the interaction between RHA vs temperature. Maximum hardness was attained at the coordinate point of 10 wt. % GP and 700 °C, equaling 196 HV. As observed in the contour plot of Fig. 14f, the optimal zone is indicated as C. When 7.1–10% GP is applied at 605–800 °C while maintaining RHA at 7.5 wt.%, a microhardness value of > 180 HV can be obtained.

3.5.5 Impact strength

Figure 15a reflects the response plot of the interaction between factor A versus B and the effect on impact strength response when temperature is held at 700 ˚C. Proportion of 3–7.5 wt. % RHA and 2–6 wt. % GP sired strength enhancement. The feat occurred on the dint of uniform distribution of the reinforcing particles. Howbeit, 7.5–12 wt. % dosage of RHA combining with 6–10 wt. % GP particles ensued deterioration in impact strength. The deterioration occurred owing to the brittle nature of the particulate. Akinwande et al. (Akinwande et al. 2022d) claimed that at higher particle density for glass powder, there is tendency for the brittle nature of the particulate to take dominance. On the basis of this, the strength starts depreciating. Studies on effect of ash particulate on impact strength of aluminum alloy has been investigated. Atuanya et al. (Atuanya et al. 2012) showcased progressive depreciation in impact strength with increasing dosage of breadfruit seed hull ash from 2 to 12 wt. % similar to occurrence between 7.5 and 12% RHA. Razzaq et al. (Razzaq et al. 2017) also reported progressive decline in impact strength of fly ash/AA 6063 composite from 2 to 12% addition similar to observation recorded between 7.5 and 12% RHA. Turning point for strength corresponding to strength value of 7.61 kJ/m^2 was attained for the interaction at 7.5 wt. % RHA and 6 wt. % GP. The two factors A and B demonstrated inverted parabolic interaction profile. The general profile of the combination is a domed-shaped profile. The contour plot in Fig. 15b highlighting the optimum zone in which strength values > 7 kJ/m^2 is realizable and depicted as A. Input of variables for such strength range is possible at the combination of 4.2–9 wt. % RHA and 3.2–7.4 wt. % GP, when maintaining temperature at 700 ˚C.

Similarly, as in the case of interaction RHA versus temperature, as it affects the impact strength response, holding GP constant at 6 wt. % (Fig. 15c), 3–7.5 wt. % RHA at stirring temperatures of 600–700 ˚C engendered strength improvement even as proportion of 7.5—12% RHA at 700–800 ˚C amounted to decrease in strength. Usman et al. (Usman et al. 2014b) compared the influence of ashes of bagasse and rice husk on properties of aluminum composite. Impact strength improved with 5–10% of the ashes corroborating the outcome revealed in present study between 3 and 7.5% RHA. The decline recorded between 7.5 and 12% RHA is in tandem with the decline showcased between 10 and 30% of the ashes. The authors discovered that RHA outperformed bagasse ash. The influence of temperature on impact strength elucidated in Mathur and Barnawal, (Mathur and Barnawal 2013) showed that temperature between 700 and 725 ˚C was synergetic to impact strength while between 725 and 750 °C, the strength value declined. The observation substantiates the findings of this study as regards how temperature affected impact strength. The decline in strength is associated with particulate coagulation, storage of residual stress owing to thermal mismatch, and occurrence of unfavorable intermetallic phases at increasing temperature. Temperature exhibited inverted parabolic interaction profile while RHA displayed a parabolic interaction profile. The two factors depicted inverted parabolic profile. Intersecting point of inflexion was reached at coded level 0 (7.5 wt. % RHA and 700 ˚C temperature) corresponding to 7.7 kJ/m^2. General profile for the interaction is assumed to be domed-shape. From the contour plot of the interaction displayed in Fig. 15d, input of

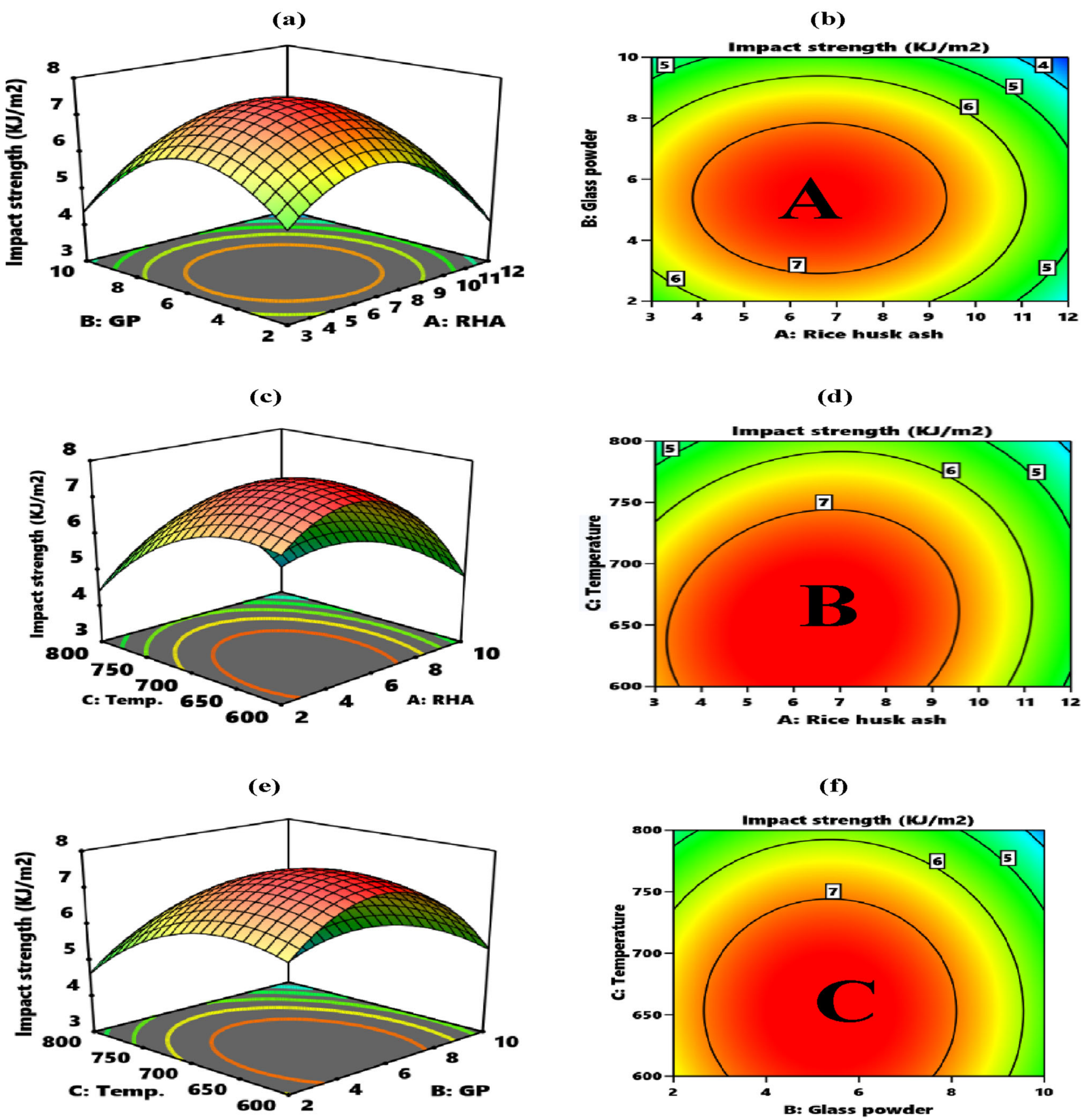

Fig. 15 Response surface and contour plots revealing effects of interactions on impact strength as represented by interactions (**a**, **b**) RHA vs GP (**c**, **d**) RHA vs temperature (**e**, **f**) GP vs temperature

3.5–9.85 RHA at 600–735 ˚C will achieve optimum strength > 7.0 kJ/m^2 MPa when holding GP constant at 6 wt. %.

Interaction GP versus temperature is demonstrated in Fig. 15e when holding RHA constant at 7.5 wt. %. GP proportion of 2–6 wt. % infused into composite at temperature between 600 and 700 ˚C led to progressive strength minimization, meanwhile, 6–10 wt. % GP at 700–800 ˚C ensued strength minimization. Ceramic reinforcement like silica added to aluminium LM-13 melt at 3, 6, 9 and 12% by authors Mallikarjuna et al. (Mallikarjuna and Basawaraj 2021) exhibited progressive enhancement in impact strength with increment in silica dosage; a feat aggreging with the trend realized between 2 and 6% GP in present investigation. Contrarily, Adediran et al. (ASTM E 9–09 2018) reported a progressive decline in impact strength as the GP content increased from 2 to 10% associated with thermal mismatch inducing residual stress in the matrix. The combined point of inflexion occurred at 6% GP and 700 ˚C temperature corresponding to 7.75 kJ/m^2. The two parameters reflected inverted parabolic interaction profile with combined domed-shaped profile. As observed in the contour plot of Fig. 15f, optimal zone is indicated as C. Impact strength > 7.0 kJ/m^2 can be obtained when 3.2–7.8% of GP is applied at 600–635 ˚C, maintaining RHA at 7.5 wt. %.

3.5.6 Compressive strength

The response plot of the interaction RHA versus GP and the outcome of the interaction on compressive strength response holding temperature at 700 °C is illustrated in Fig. 16a. Particulate loading of 2–7.5 wt. % RHA and 2–10 wt. % GP prompted strength enhancement ascribable to condensed and reduced interparticle distance based on the even dispersion of the particles within the matrix, resulting in increased dislocation density, consequently improving strength. Authors Saravanan and Kumar (Saravanan and Kumar 2013) demostrtaed the potential of RHA in enhancing the compressive strength of the AlSi10Mg matrix as assimilation of 2–12% RHA in the matrix enhanced compressive strength. The outcome of Ali and Motgi (Ali and Motgi 2021) disclosed that the combination of RHA and ceramic particulate like SiC has the potential to improve the performance of aluminum matrix. The outcomes reported by Fenghong et al. (Fenghong et al. 2019) delineate the impact of tungsten carbide and silica carbide in improving the strength of the Al 6061 matrix. In contrast, 7.5–12 wt. % dosage of RHA interacted with 2–10 wt. % GP particles provoked a decrease in response on account of agglomeration and clustering of particles encouraging stress concentration within the matrix. The maximum compressive strength for the interaction is 701.4 MPa, corresponding to 7.5% RHA and 10% GP. The two factors, A and B, manifested an inverted parabolic interaction profile, portraying a combined domed-shaped profile. In Fig. 16b, region A is the optimum zone as regards the interaction between RHA and GP. At a constant temperature of 700 °C, a feasible RHA dosage of 6.9–8.1 wt.% and GP loading of 9.9–10 wt.% at a constant temperature of 700 °C.

Regarding the interaction RHA versus temperature, as it affects the compressive strength response at constant GP of 6 wt.% (Fig. 16c), 3–7.5 wt.% RHA at temperatures of 600–700 °C resulted in an improvement in the response, whereas particulate loading of 7.5–12% RHA used at temperatures of 700–800 °C resulted in a decrease in strength. Such an improvement in strength is attainable and happened on account of enhanced closed packing within the composite structure, consequently improving compaction. Saravanan and Senthilkumar (Saravanan and Senthilkumar 2014) reported a progressive rise in the compressive strength of aluminum composites prepared with 2–12 wt.% RHA. The blend of fly ash and RHA as reported by Senapati et al. (Senapati et al. 2017) has considerable input in improving the compressive strength of the Al-Si LM6 alloy. The temperature profile depicted in this study as regards compressive strength is similar to the inverted parabolic profile delineated in Akinwande et al. (Akinwande et al. 2022e), as temperatures between 500 and 600 °C enhanced the compressive strength of Al 6061 while temperatures between 600 and 700 °C spawned a decrease in the strength. The decrease in strength as a result of higher temperatures is traced to the presence of defected and delirious intermetallic phases imbibed as a result of high-temperature casting. The two variable factors manifested an inverted parabolic interaction profile and the point of intersecting for the inflexions was reached at a coordinate of 7.5 wt.% RHA and 700 C temperature, corresponding to 571.5 MPa. The general profile for the interaction is a domed shape profile. From the contour plot of the interaction displayed in Fig. 16d, an input of 4.8–8.3 RHA at 630–730 °C will achieve an optimum result of strength > 600 MPa, holding GP constant at 6 wt.%.

Figure 16e depicts the GP versus temperature interaction at a constant RHA of 7.5 wt.%. Compressive strength triggering strength improvement requires a GP proportion of 2–10 wt.% incorporated at a temperature range of 600 and 700 °C. Findings showcased by Adediran et al. (ASTM E 9–09 2018) depicted the presence of GP in the Al 6061 matrix ensued enhancement of compressive strength, giving an optimum value at 8% infusion. Similarly, Meignanamoorthy et al. (Meignanamoorthy et al. 2022) used a stir casting process to reinforce an Al–Si–Mg alloy with nano aluminum nitride particles at a dosage of 2–12%. Tungsten carbide (WC) is another ceramic particulate that has been tested on the compressive strength of aluminum alloy, as noted by Swamy et al. (Swamy et al. 2011). Investigations undergone by Prajval and Prasad (Prajval and Prasad 2016) revealed the combination of the improvement effect of the blend of RHA and ceramic particulates such as titanium dioxide particles on the compressive strength of aluminum A 356 alloy. Interactivity between 2 and 10 wt.% GP at temperatures ranging from 700 to 800 °C, on the other hand, causes strength reduction as a result of induced residual stress based on particle clusters. While glass powder exhibited a positive linear interaction profile, temperature portrayed an inverted parabolic profile. Maximum compressive strength for the interaction occurred at 10% GP and 700 °C, corresponding to 704.1 MPa. As observed in the contour plot of Fig. 16f, the optimal zone is indicated as C. Compressive strength > 700 MPa can be realized when 9.9–10 wt.% of GP is applied within a temperature range of 665–680 °C, maintaining RHA at 7.5 wt.%.

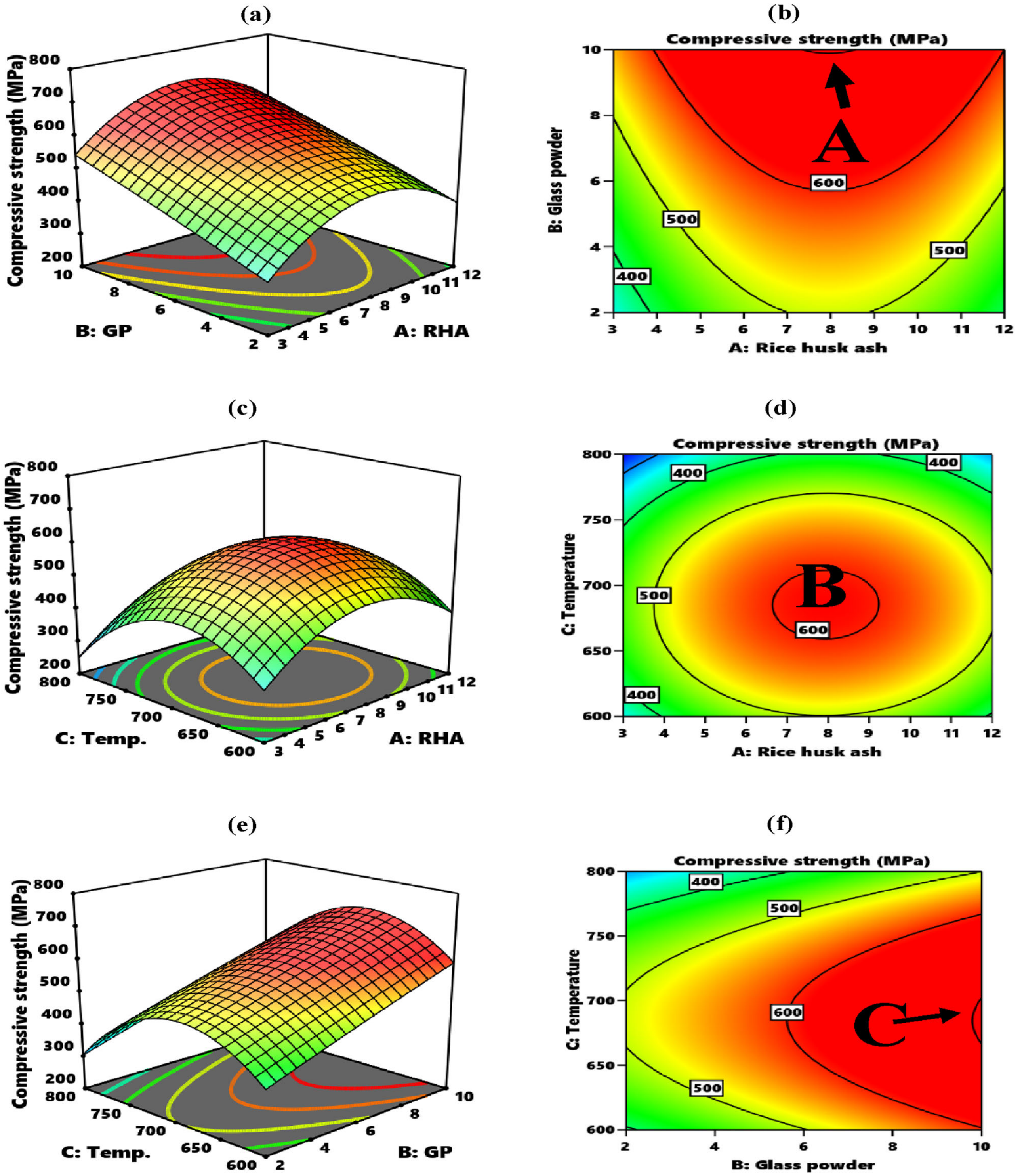

Fig. 16 Response surface and contour plots revealing effects of interactions on compressive strength as represented by interactions (**a**, **b**) RHA vs GP (**c**, **d**) RHA vs temperature (**e**, **f**) GP vs temperature

3.6 Optimization and validation

Response surface methodology is a good statistical and mathematical tool for optimization of multi-response characteristics predetermined via constraints Awolusi et al. (Awolusi et al. 2020) and has found application in a series of optimization studies (Shihab et al. 2021; Premnath et al. 2012; Penjumras et al. 2015; Simsek et al. 2015; Bakhtiari et al. 2020; Akinwande et al. 2023c). In the present study, expert design 13 was utilized in carrying out a multi-objective optimization procedure with the stipulated criteria indicated in Table 10. The input variables of A, B, and C were set in a range (Table 10) while the main goal was to maximize the strength parameters.

The optimum experimental conditions for the multi-response optimization as prtedicted by the software are 7.24185 ~ 7.2 wt. % RHA, 6.21163 ~ 6. wt. % GP and 695.126 ~ 695 ˚C for temperature (Fig. 17). The predicted response values are 614.66 MPa, 700.662 MPa, 548.977 MPa, 174.367 Hv, 7.55 kJ/m^2, and 611.165 MPa for yield tensile strength, ultimate tensile strength, flexural strength, microhardness, impact strength, and compressive strength, respectively (Table 10). In the validation of the model, a confirmation experiment was carried out at optimum conditions of 7.2% RHA, 6.2% GP, 695 ˚C and triplicate samples were tested for each property. Experimental values obtained are 603.4 MPa, 697.3 MPa, 556.1 MPa, 183 Hv, 7.7 kJ/m^2, and 598.3 MPa for yield tensile strength, ultimate tensile strength, flexural strength, microhardness, impact strength, and compressive strength in that order. The estimated errors for each of the five responses are less than 5%, confirming the models to be statistically fit for the prediction of responses.

3.7 Desirability function for each response and overall desirability function

The desire function involves transformation of the multi-response functions into a definite function with the goal of optimizing each response (Akinwande et al. 2023c). The overall desirability function, which combines the desirability of each function into values, usually varies between 0 and 1

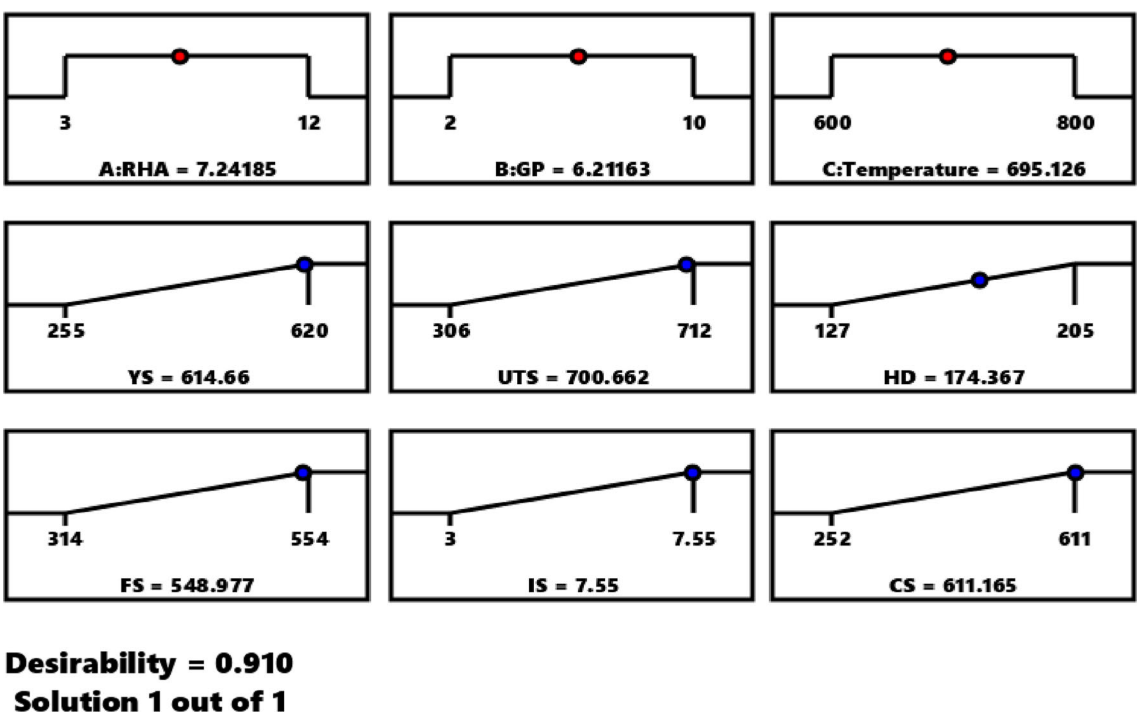

Fig. 17 Optimization ramp

Table 10 Optimization criteria

Name	Goal	Lower Limit	Upper Limit	Lower Weight	Upper Weight
A: RHA	Is in range	3 wt. %	12 wt. %	1	1
B: GP	Is in range	2 wt. %	10 wt. %	1	1
C: temperature	Is in range	600 ˚C	800 ˚C	1	1

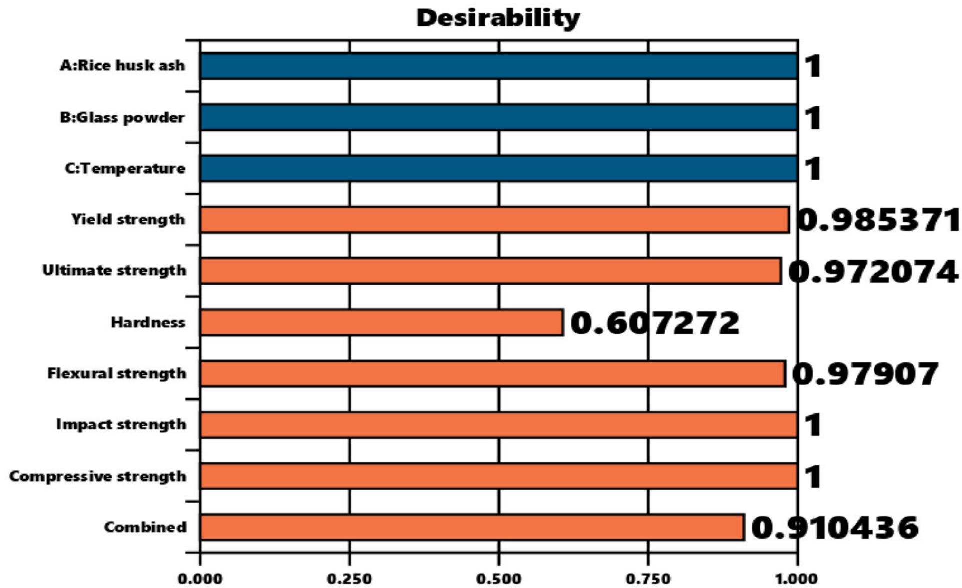

Fig. 18 Desirability values for each factor, responses and combined

Table 11 Validation table

Properties	Predicted values	Confirmation values	% Error
Yield tensile strength (MPa)	614.66	603.4	− 1.87
Ultimate tensile strength (MPa)	700.662	697.3	− 1.91
Flexural strength (MPa)	548.977	556.1	+ 1.30
Microhardness (Hv)	174.367	183	+ 4.95
Impact strength (KJ/m^2)	7.55	7.7	+ 2.12
Compressive strength	611.165	598.3	− 2.10

(Akinwande et al. 2023c). The desirability of all responses is above 0.9, except for hardness (Fig. 18). This indicates that the strong properties have very good desirability. Moreso, the models are highly dependable in the prediction of responses within the design space. Hardness portrayed a desirability of 0.607, indicating 60.7% desirability. Though the desirability (for hardness) is greater than 50% when compared to the strength factors, it is low, as evidenced by the 4.95% error in Table 11. Hence, the model for hardness is not highly dependable for prediction. A combined value of 0.91 was obtained for the desirability, a high value assuming a 91% desirability, depicting the optimum conditions are highly dependable. Additionally, it indicates that the models of multi-response optimization are highly desirable, therefore the validation values are results obtained via the model that have high dependability.

4 Conclusions

The Box-Behnken approach of the response surface method was employed in the design of experiments and optimization of mechanical performance of Al-7075 hybridized with green fillers (RHA and GP). We conclude that.

1. 1.The green fillers and stirring temperature played important roles in the features observed in the morphology. Moreso, the performance of the specimen is attributed to its microstructural features.
2. Major phases identified between 700 and 800 °C are the base Al phases, and SiO2 secondary phases attained as a result of the addition of the reinforcing particles. At 800 °C, intermetallics were identified owing to high-temperature reactions.
3. ANOVA analysis showed that the three parameters; RHA proportion, GP dosage and stirring temperature, had significant effects on yield, ultimate tensile, flexural and impact strengths as well as micro hardness as the probability value was less than 0.05 for each response.
4. The model developed for each response parameter was affirmed to be statistically significant and fit for prediction of the responses. Meanwhile, the response surface plot showed that each response is dependent on the interactive pattern between the factors.
5. The optimum experimental condition for the multi-response optimization is 0.28 wt. % RHA, 8.47 wt. % GP, and 598.06 C for temperature. The predicted values are 614.66 MPa, 700.662 MPa, 548.977 MPa, 174.367 Hv, and 7.55 KJ/m^2 for yield tensile strength, ultimate tensile strength, flexural strength, microhardness, impact strength, and compressive strength respectively.

The validation experiment yielded values of 603.4 MPa, 697.3 MPa, 556.1 MPa, 183 Hv, and 7.7 KJ/m^2, and 598.3 MPa respectively, validating the model.

Hence, the validation procedure engaged in affirmed the models to be significant and the response surface methodology method is capable of the optimization procedure.

Acknowledgements The authors appreciate the Center for Functional Nano-Ceramics, National University of Science and Technology, "MISIS", 119049, Lenin av., 4, Moscow, Russia and Department of Materials Science and Engineering, University of Virginia, Charlottesville, VA 22904, USA.

Author contributions AA Akinwande, OS Adesina: Conceptualization, data curation, methodology, formal analysis, article writing and literature review, manuscript draft, editing. AA Adediran, OO Sanyaolu, OA Balogun: data curation, article writing and literature review, manuscript draft, editing. V Romanovski: methodology, formal analysis, article writing and literature review, manuscript draft, editing.

Funding The authors receive no funding from any organization.

Data availability All data generated or analyzed during this report are included in this published article.

Declarations

Conflict of interest The authors declare no conflict of interest that may influence representation or interpretation of reported research results.

References

Abraham SJ, Dinaharan I, Selvam JDR, Akinlabi ET (2019) Microstructural characterization of vanadium particles reinforced AA6063 aluminium matrix composites via friction stir processing with improved tensile strength and appreciable ductility. Composites Commun 12:54–58. https://doi.org/10.1016/j.coco.2018.12.011

Adediran AA, Balogun OA, Akinwande AA, Adesina OS, Bello OS (2021a) Influence of waste glass and particulate coconut shells as reinforcement materials in the production of masonry bricks. J Materials Civ Eng 33(10):1–14. https://doi.org/10.1061/(ASCE)MT.1943-5533.0003903

Adediran AA, Akinwande AA, Balogun OA, Olorunfemi BJ, Kumar MS (2021b) Optimization studies of stir casting parameters and mechanical properties of TiO2 reinforced AL 7075 composite using response surface methodology. Sci Rep 11(1):19860. https://doi.org/10.1038/s41598-021-99168-1

Adediran AA, Akinwande AA, Balogun OA, Bello OS, Akinbowale MK, Adesina OS, Ojo AA (2022) Mechanical and optimization studies of polypropylene hybrid biocomposites. Sci Rep 12(2468):1–18. https://doi.org/10.1038/s41598-022-06304-6

Adeleke A A, Ikubanni P P, Orhadahwe T A, Christopher C T, Akano J M, Agboola O O, Adegoke S O, Balogun A O, Ibikunle R A, (2021). Sustainability of multifaceted usage of biomass: a review. Heliyon. 7(2021): e08025. j.heliyon.2021.e08025

Ademokoya O, Adama K (2017) Glass-fiber reinforced composites: the effect of fiber loading and orientation on tensile and impact strength. Niger J Technol 36(3):782–787. https://doi.org/10.4314/njt.v36i3.17

Adesina OS, Akinwande AA, Balogun OA, Adediran AA, Sanyaolu OO, Romanovski V (2023) Statistical analysis and optimization of the experimental results on performance og green aluminium-7075 hybrid composites. J Composite Sci 7(3):115. https://doi.org/10.3390/jcs7030115

Ahamed AA, Ahmed R, Hossain MB, Billah, (2016) Fabrication and characterization of aluminium-rice husk ash composites prepared by stir casting method. Rajshahi Univ J Sci Eng 44:9–18

Akinwande AA, Adediran AA, Balogun OA, Olusoju OS, Adesina OS (2021) Influence of alkaline modification on selected properties of banana fiber paperbricks. Sci Rep 11(5793):1–19. https://doi.org/10.1038/s41598-021-85106-8

Akinwande AA, Balogun OA, Romanovski V, Danso H, Ademati OA, Adetula YV (2022a) Recycling of synthetic waste wig fiber in the production of cement-adobe for building envelope: physio-hydric properties. Environ Sci Pollut Res. https://doi.org/10.1007/s11356-022-18649-6

Akinwande AA, Balogun OA, Romanovski V, Danso H, Kamarou M, Ademati AO (2022b) Mechanical performance and Taguchi optimization of kenaf fiber/cement-paperboard composite for interior application. Environ Sci Pollut Res. https://doi.org/10.1007/s11356-022-19449-8

Akinwande AA, Folorunso DO, Balogun OA, Romanovski V (2022c) Mathematical modelling, multi-objective optimization, and compliance reliability of paper derived eco-composites. Environ Sci Pollut Res. https://doi.org/10.1007/s11356-022-20714-z

Akinwande AA, Balogun OA, Romanovski V (2022d) Modelling, multi-response optimization, and performance reliability of green metal composites produced from municipal wastes. Environ Sci Pollut Res. https://doi.org/10.1007/s11356-022-20023-5

Akinwande AA, Adesina OS, Adediran AA, Balogun OA, Mukuro D, Balogun OP, Tee KF, Kumar MS (2023a) Microstructure, process optimization, and strength modeling of green-aluminium-6061 composite as automobile material. Ceramics 6(1):386–415. https://doi.org/10.3390/ceramics6010023

Akinwande AA, Moskovskikh D, Romanovskaia E, Balogun OA, Kumar JP, Romanovski V (2023c) Applicability of extreme vertices design in the compositional optimization of 3D-printed lightweight high-entropy-alloy/B4C/ZrO2/titanium trihybrid aero-composite. Math Comput Appl 28:54. https://doi.org/10.3390/mca28020054

Akinwande AA, Adediran AA, Balogun OA, Yibowei ME, Barnabas AA, Talabi HK, Olorunfemi BJ, (2022e) Optimization of selected casting parameters on the mechanical behavior of Al 6061/glass powder composites. Heliyon. 8(2022e): e09350. j.heliyon.2022e.e09350.

Akinwande AA, Balogun OA, Adediran AA, Adesina OS, Romanovski V, Jen TC, 2023b Experimental analysis, sttaistical modeling, and pareametric optimization of quinary-(CoCrFeMnNi)100-x/TiCx high-entyropy-alloy (HEA) manufacturing by laser additive manufacturing. Results Eng. 17:100802. https://doi.org/10.1016/j.rineng.2022.100802.

Ali S A, Motgi B S, (2021) A study on mechanical properties of Al 6068 based metal matrix composite reinforced with rice husk ash (RHA) and silicon carbide (SiC). Int J Modern Trends Sci Technol. 7(9): 71–78. https://doi.org/10.46501/IJMTST0709012

Anyalem GF (2020a) (2020) Processing methods and mechanical properties of aluminium matrix composites. Adv Material Sci Eng 3765791:1–19. https://doi.org/10.1155/2020/3765791

Anyalem GF (2020b) (2020) Processing methods and mechanical properties of aluminum matrix composites. Adv Mater Sci Eng 3765791:1–19. https://doi.org/10.1155/2020/3765791

Arunachalam R, Krishnan PK, Muraliraja R (2019) A review on the production of metal matrix composites through stir casting-furnace design, properties, challenges, and research opportunities.

J Manuf Process 42(2019):213–245. https://doi.org/10.1016/j.jmapro.2019.04.017
ASTM A 370–20, (2020) Standard test methods and definitions for mechanical testing of steel products. ASTM International, West Conshohocken, PA, 2020. https://doi.org/10.1520/A0370-21.
ASTM E 3–11, (2017) Standard guide for preparation of metallographic specimens. ASTM International, West Conshohocken, PA, 2017. https://doi.org/10.1520/E0003-11.
ASTM E 384–17, (2017) Standard test methods for micro-identation hardness of materials.ASTM International, West Conshohocken, PA, 2017. https://doi.org/10.1520/E0384-17.
ASTM E 8/E8M-21,(2021) Standard test methods for tension testing of metallic materials. ASTM International, West Conshohocken, PA, 2021. https://doi.org/10.1520/E008M-16.
ASTM E 9–09, (2018) Standard test method of compression testing of metallic materials at room temperature. ASTM International, West Conshohocken, PA, 2018. https://doi.org/10.1520/E0009-09.
Atuanya CU, Ibhadode AOA, Dagwa IM (2012) Effects of breadfruit seed hull ash on the microstructures and properties of Al-Si-Fe alloy/breadfruit seed hull ash particulate composites. Results Phys 2(2012):142–149. https://doi.org/10.1016/j.rinp.2012.09.003
Awolusi TF, Oke LO, Akinkurolere OO, Uban DP, Bamisaye RT, Aluko OG (2020) The application of response surface methodology in understanding the compressive strength and water absorption capacity of sandcrete. SILICON. https://doi.org/10.1007/s12633-020-00701-0
Bakhtiari A, Ghasemi FA, Naderi G, Nakhaei MR (2020) An approach to the optimization of the mechanical properties of polypropylene/nitrile butadiene rubber/halloysite nanotube/polypropylene-g-maleic anhydride nanocomposites using response surface methodology. Polym Compos 2020:1–14. https://doi.org/10.1002/pc.25541
Balogun O A, Akinwande A A, Adediran A A, Ogunsanya O A, Ademati A O, Kumar M S, Erinle T J, Akinlabi E T, (2022a) Microstructure and particle size effects on selected mechanical properties of waste glass-reinforced aluminium matrix composites. Materials Today. https://doi.org/10.1016/j.matpr.2022.05.330
Balogun O A, Akinwande A A, Ogunsanya O A, Ademati A O, Adediran A A, Erinle T J, Akinlabi E T, (2022b) Central composite design and optimization of selected stir casting parameters on flexural strength and fracture toughness of mTiO2p/Al 7075 composites. Materials Today. https://doi.org/10.1016/j,matpr.2022.05.315
Barbosa J, Puga H, Oliveira S, Ribeiro S, Prokic M, (2014) Physical modification of intermetallic phases in Al–Si–Cu alloys. 148(2014): 1163-1170. https://doi.org/10.1016/j.matchemphys.2014.09.041
Bharathi V, Ramachandra M, Srinivas S (2017) Influence of fly ash content in aluminium matrix composite produced by stir-squeeze casting on the scratching abrasion resistance, hardness and density levels. Mater Today 4(8):7397–7405. https://doi.org/10.1016/j.matpr.2017.07.070
Bian Y, Gao T, Zhao Y, Liu G, Liu X (2020) Synthesis of an Al-based composite reinforced by multi-phase ZrB_2, Al_3BC and Al_2O_3 with good mechanical and thermal properties at elevated temperature. Materials 13(4048):1–10. https://doi.org/10.3390/ma13184048
Boopathi M, Arulshri MPK, Iyandurai N (2013) Evaluation of mechanical properties of aluminium alloy 2024 reinforced with silicon carbide and fly ash hybrid metal matrix composiotes. Am J Appl Sci 10(3):219–229. https://doi.org/10.3844/ajassp.2013.219.229
Bulei C, Todor M P, Kiss I, Alexa V, (2019) Aluminium matrix composites: processing of matrix from re-melted aluminium wastes in micro-melting station. IOP Conference Series: Materials Science and Engineering. 477(2019): 012049. https://doi.org/10.1088/1757-899x/477/1/012049.
Canakci A, Arslan F, Varol T, (2014) Physical and mechanical properties of stir-casting processed $AA2024/B_4Cp$ composites. Scienmce Eng Composite Materials. 21(4): 505 – 515. 10.1515secm-2013-0118
Cao H, Wang C, Che J, Luo Z, Wang L, Xiao L, Wang J, Hu T (2019) Effect of flow state of pure aluminium and A 380 alloy on porosity of high pressure die castings. Materials 12(4219):1–18. https://doi.org/10.3390/ma12244219
Chinta ND, Selvaraj N, Mahesh V (2018) Mechanical characterization of aluminium-red mud metal matrix composites. Mater Today 5(13):26911–26917. https://doi.org/10.1016/j.matpr.2018.08.178
Das D, Roy DK, Satpathy MP, Nanda BK, Nayak RK (2019) Compressive, impact and flexural behavior of Al based metal matrix composites. Materials Today 18(2019): 3080–3086. j.matpr.2019.07.180
Dhaneswara D, Fatriansyah JF, Ramadhan R, Ashari A (2019) The effect of melting temperature on aluminium metal casting using mixed degasser-based sodium fluoride and sodium nitrate. MATEC Web of Conference 269(07001):1–7. https://doi.org/10.1051/matecconf/201926907001
Dwivedi SP, Sharma S, Mishra RK (2016) Synthesis and mechanical behavior of green metal matrix composites using waste eggshells as reinforcement materials. Green Process Synthesis. https://doi.org/10.1515/gps.2016-0006
Edoziuno F O, Nwaeju C C, Adediran A A, Odoni B U, Prakash V R A, (2021). Mechanical and microstructural characteristics of aluminium 6063 alloy/palm kernel shell composites for light weight application. Scientific African 12(2021), e00781. https://doi.org/10.1016/j.sciaf.2021.e00781
El-Mahallawi IS, Shash AY, Amer AE (2015) Nanoreinforced cast Al–Si alloys with Al2O3, TiO2 and ZrO2 nanoparticles. Metals 5(2):802–821. https://doi.org/10.3390/met5020802
Fenghong C, Chang C, Zhenyu W, Muthuramalingam T, Anbuchezhiyan G (2019) Effects of silicon carbide and tungsten carbide in aluminium metal matrix composites. SILICON. https://doi.org/10.1007/s12633-018-00516
Ferreira IL, De Castro JA, Garcia A (2019) On the prediction of temperature-dependent viscocity of multicomponent liquid alloys. Continuum Mech Thermodyn 31:1369–1385. https://doi.org/10.1007/s00161-019-00753-7
Gangwar S, Patnaik A, Yadav P C, Sahu S, Bhat I K, (2019) Development and properties evaluation of marble dust reinforced ZA-27 alloy composites for ball bearing application. 6(2019): 076525. https://doi.org/10.1088/2053-1591/ab1362
Gikunoo E, Omotoso O, Oguocha INA (2013) Effect of fly ash particles on the mechanical properties of aluminium casting alloy A 535. Mater Sci Technol 21(2):143–152. https://doi.org/10.1179/174328405X18601
Gladston JAK, Sheriff NM, Dinaharan I, Selvan JDR (2015a) Production and characterization of rice husk ash particu;late reinforced AA 6061 aluminium alloy composites by compocasting. Trans Non-Ferrous Metallurgical Soc China 25(2015):683–691. https://doi.org/10.1016/S1003-6326(15)63653-6
Gladston JAK, Sheriff NM, Dinaharan I, Selvam JDR (2015b) Production and characterization of rice husk ash particulate reinforced AA6061 aluminium alloy composites by compocasting. Trans Nonferrous Metals Soc China 25(2015):683–691. https://doi.org/10.1016/S1003-6326(15)63653-6
Hayajneh MT, Almomani MA, Al-Shrida MM (2019) Effects of waste eggshell addition on microstructures, mechanical and tribological properties of green metal matrix composite. Sci Eng Composites Materials. https://doi.org/10.1515/gps-2016-0006
Hendronursito Y, Ojahan T, Anshori A, Yunanto A, (2020) Optimization of stir casting of aluminium matrix composites (AMCs) with filler of recycled glass powder (RGP) for the mechanical properties. J Mech Eng Sci Technol. 4(2):101–114. https://doi.org/10.17977/um016v4i22020p101.

Hirsch J (2011) Aluminium in innovative light-weight car design. Mater Trans 52(5):818–824. https://doi.org/10.2320/matertrans.L-MZ201132

Hirsch J (2014) Recent development in aluminium for automotive application. Trans Nonferrous Metals Soc China 24(2014):1995–2002. https://doi.org/10.1016/S1003-6326(14)63305-7

Ikubanni PP, Oki M, Adeleke AA (2020) A review of ceramic/bio-based hybrid reinforced aluminium matrix composites. Cogent Engineering 7(1):1727167. https://doi.org/10.1080/23311916.2020.1727167

Imran M, Khan ARA, Megeri S, Sadik S (2016) Study of hardness and tensile strength of aluminium-7075 percentage varying reinforced with graphite and bagasse-ash composites. Resource-Efficient Technol 2(2016):81–88. https://doi.org/10.1016/j.reffit.2016.06.007

Joseph OO, Babaremu KO (2019) Agricultural waste as a reinforcement particulate for aluminium metal matrix composites (AMMCs): a review. Fibers 7(33):1–9. https://doi.org/10.3390/fib7040033

Khan M. Z, Anas M, Hussain A, Haque M I, Rasheed K. (2015) Effect on mechanical properties of aluminium alloy composites on adding ash as reinforcement material. 25(2): 1–7. https://doi.org/10.14456/jmmm.2015.9

Kim BJ, Jung SS, Hwang JH, Park YH, Lee YC (2019) Effect of eutectic Mg_2Si phase modification on the mechanical properties of Al-8Zn-6Si-4Mg-2Cu cast alloy. Metals. 9(32): 1–10. 3390/met9010032

Klemens A, Rahangmetan C, Sariman F, Syahid M (2019) Study on effect of temperature smelting and pouring to mechanical properties Aluminium 7075. IOP Conf Ser 343(012166):1–5. https://doi.org/10.1088/1755-1315/343/1/012166

Kolappan S, Arunkumar T, Mohanavel V, Subramani K, Kailasanathan C, Kumaran P, Subbiah R, Kumar S S, (2022). Experimental investigation on stir casted hybrid composite AA 7068 with Snd coconut shell fly ash. Materials Today. https://doi.org/10.1016/j.matpr.2022.04.359

Krupakara PV, Ravikumar HR (2015) Corrosion characteristics of aluminium 6061/red mud metal matrix composites in sea water. Int J Adv Res Chem Sci 2(6):52–55

Kulkami PP, Siddeswarappa B, Kumar KSH (2019) A survey of effect of agro waste ash as reinforcement on aluminium base metal matrix composites. J Compos Mater 9(3):312–326. https://doi.org/10.4236/ojcm.2019.93019

Kulkarni P P, Siddeswarappa B, (2022). A study on microstructure and mechanical behaviour of AA 6063 metal matrix composites reinforced with areca shealth ash and rice husk ash. Materials Today. 52(3): 445–451. https://doi.org/10.1016/j.matpr.2021.09.104.

Kumar A, Kumar M (2022) Fracture toughness and thermal investigations of Al 7075-cobalt particulates reinforced alloy composites prepared using high vacuum casting method for gear applications: proposed thermal conductivity and fracture toughness modeling. Int J Metal Casting. https://doi.org/10.1007/s40962-022-00901-x

Kumar A, Kumar V, Kumar A, Nahak B, Singh R (2021) Investigation of mechanical and tribological performance of marble dust 7075 aluminium alloy. Mater Today 44(6):4542–4547. https://doi.org/10.1016/j.matpr.2020.10.812

Kumar A, Kumar M, Pandey B (2022b) Investigations on mechanical and sliding wear performance of AA7075 – SiC/Marble dust/Graphite hybrid alloy composites using hybrid entropy - vikor method. SILICON 14:2051–2065. https://doi.org/10.1007/s12633-021-00996-7/2021

Kumar A, Kumar M, Gothwal S, Srivastava P (2022c) Analysis of the sliding wear (Experimental and Modeling Validation), thermal, thermo-mechanical, and fracture performance of AA7075-chromium alloy composites. J Bio- Tribo-Corrosion 8:107. https://doi.org/10.1007/s40735-022-00705-w

Kumar MS, Akinwande AA, Yang SH, Margabandu V, Romanovksi V (2023) Investigation on mechanical behavior of Al-Mg-Si alloy hybridized with calcined eggshell and TiO2 particulates. Biomass Conversion Biorefinery. https://doi.org/10.1007/s13399-023-04215-8

Kumar A., Patnaik A., Bhat I. K., 2010. Tribology analysis of Cobalt particulate filled Al 7075 Alloy for gear materials: A Comparative study. Silicon Vol. 11/ 1295–1311(2019) https://doi.org/10.1007/s12633-018-9920-2.

Kumar M.; Kumar R.; Bhaskar S.; Kumar A.; Harizan S., 2022a. Parametric optimization and ranking analysis of hybrid AA2024-SiC/Si3N4 alloy composites based on mechanical and sliding wear performance. Journal of Bio and Tribo –Corrosion, 8, 24 https://doi.org/10.1007/s40735-021-00619-z

Kumar A., Kumar M., Tiwari A. T., 2022d. Analysis of mechanical and sliding wear performance of hybrid AA7075-SiC/Gr/Cu alloy composites fabricated by high vacuum stir casting process. Journal of Bio and Tribo –Corrosion; 8: 12 https://doi.org/10.1007/s40735-021-00606-4.

Lei Z (2012) Research on mechanical properties of the waste glass/waste aluminium wearable materials. Adv Materials Res 460(2012):424–427. https://doi.org/10.4028/www.scientific.net/AMR.460.424

Madhankumar S., Rajesh S, Vignesh T, Harikrishnan M, (2018) Fabrication of Al 6082, SiC and Boron glass powder composites and evaluation of mechanical properties. Int J Innovative Res Sci Eng Technol. 7(1): 51–58 https://doi.org/10.15680/IJIRSET.2017.0701003

Mallikarjuna GB, Basawaraj E (2021) Tensile and impact behavior of Al-silica metal matrix composites. Int J Sci Eng Res 12(2):61–66

Mathur S, Barnawal A (2013) Effect of process parameter of stir casting on metal matrix composites. Int J Sci Res 2(12):395–398

Meignanamoorthy M, Mohanavel V, Velmurugan P, Ravichandran M, Alonazi WB, Sivakumar S, Gebrekidan AM (2022) (2022) Effect of nanoaluminium nitride ceramic particles on microstructure, mechanical wear, and machining behavior of Al–Si–Mg alloy matrix composites produced by bottom pouring type stir casting route. J Nanomater 5013914:1–14. https://doi.org/10.1155/2022/5013914

Mishra P, Mishra P, Rana R S, (2017). Effect of rice husk ash reinforcement on mechanical properties of aluminium alloy (LM 6) matrix composites. 5(2018): 6018–6022. https://doi.org/10.1016/j.matpr.2017.12.205

Moses JJ, Dihaharan I, Sekhar SJ (2016) Prediction of influence of process parameters on tensile strength of AA6061/TiC aluminium matrix composites produced using stir casting. Trans Nonferrous Metals Soc China 26(2016):1498–1511. https://doi.org/10.1016/S1003-6326(16)64256-5

Mozammil S, Verma R, Karloopia J, Jha PK (2020) Investigation and measurement of porosity in Al + 4.5Cu/6 wt. % TiB_2 in situ composite: Optimization and statistical modelling. J Market Res 9:8041–8057. https://doi.org/10.1016/j.mrt.2020.05.045

Mukherjee A, Ghosh M, Mondal K, Venkitanarayanan P, Moon A P, Varshney A, (2015) Study of mechanical properties, microstructure and corrosion behavior of Al 7075 T651 alloy with varying strain rate. IOP Conference Series. 75(2015): 012031. https://doi.org/10.1088/1757-899X/75/1/012031.

Myalska-Glowacka H, Chmiela B, Godzierz M, Sosanska M (2022) Residual stress induced by addition of nanosized TiC in titanium matrix composites. Materials 15(2517):1–15. https://doi.org/10.3390/ma15072517

Nandy S, Fortunato E, Martins R (2022) Green economy and waste management: an inevitable plan for materials science. Progress Nat Sci 32(2022):1–9. https://doi.org/10.1016/j.pnsc.2022.01.001

Ogunbiyi O., Tian Y., Akinwande A. A., Rominiyi A. L., 2023. AA7075/HEA composites fabricated by microwave sinetring: assessment of the microstructural features and response surface optimization. Intermetallics. 155, 107830. https://doi.org/10.1016/j.intermet.2023.107830.

Ogunsanya OA, Akinwande AA, Balogun OA, Romanovski V, Kumar MS (2022) Mechanical and damping behavior of artificially aged Al 6061/TiO2 reinforced composites for aerospace application. Part Sci Technol. https://doi.org/10.1080/02726351.2022.2065652

Ogunsanya OA, Akinwande AA, Radhakrishnan RM, Talabi HK, Kumar MS, Margabandu V, Bhowmik A (2023) Experimental investigation on the mechanical performance of the Al2O3 and ZrO2 added Al-Mg-Si alloy for structural applications. J Process Mech Eng. https://doi.org/10.1177/09544089231159777

Pai A, Shankar S, D'Silva RE, Nikhil RG (2015) Effect of graphite and granite dust particulates as micro-fillers on tribological performance of Al 6061–T6 hybrid composites. Tribol Int. https://doi.org/10.1016/j.triboint.2015.07.035

Panda B, Niranjan C A, Vishwanatha A D, Harisha P, Chandan K R, Kumar R, (2020), Development of novel stir cast aluminium composite with modified coconut shell ash filler. Materials Today. 22(4): 2715-2724. j.matpr.2020.03.402

Pareez B, Malaque MA, Jamal NA (2021) Influence of agro-based reinforcements on the properties of aluminium matrix composites: a systematic review. J Material Sci. https://doi.org/10.1007/s10853-021-06305-2

Penjumras P, Rahman RA, Talib RA, Abdan K (2015) (2015) Response surface methodology for the optimization of preparation of biocomposites based on poly(lactic acid) and durian peel cellulose. Scientific World J 293609:1–12. https://doi.org/10.1155/2015/293609

Prajval S, Prasad PR (2016) Synthesis and evaluation of tensile and compression strength of aluminium A356 reinforced with rice husk ash and TiO_2 particle. Int J Sci Res Publ 6(10):132–136

Premnath AA, Alwarsamy T, Rajmohan T (2012) Experimental investigation and optimization of process parameters in milling of hybrid metal matrix composites. Materials Manuf Process 27(10):1035–1044. https://doi.org/10.1080/10426914.2012.677911

Razzaq AM, Majid DL, Ishak MR, Basheer, (2017) Effect of fly ash addition on the physical and mechanical properties of AA6063 alloy reinforcement. Metals 7(477):1–15. https://doi.org/10.3390/met7110477

Roether J A and Boccaccini A R, (2005) Dispersion-reinforced glass and glass-ceramic matrix composites. In: NP Bansal (eds) Handbook of ceramic composites. Springer, Boston, MA. https://doi.org/10.1007/0-387-23986-3_20.

Saini P, Singh PK (2022) Studies on microstructure characteristics and mechanical properties of hybrid Al-4032 AMC reinforced with SiC and granite marble powder. Proc Inst Mech Eng C J Mech Eng Sci. https://doi.org/10.1177/09544062211065342

Saravanakumar A, Sasikumar P (2018) Flexural behavior and microstructure of hybrid metal matrix composites. J Mater Environ Sci. 9(10): 2951–2955. http://www.jmaterenvironsci.com

Saravanan SD, Kumar MS (2013) Effect of mechanical properties on rice husk ash reinforced aluminium alloy (AlSi10Mg) matrix composites. Proc Eng 64(2013):1505–1513. https://doi.org/10.1016/j.proeng.2013.09.232

Saravanan SD, Senthilkumar M (2014) Mechanical behavior of aluminium (AlSi10Mg)-RHA composite. Int J Eng Technol 5(6):4834–4840

Saravanan SD, Senthilkumar M, Shankar S (2013) Effect of particle size on tribological behaviour of rice husk ash-reinforced aluminium alloy (AlSi10Mg) matrix composites. Tribol Trans 56:1156–1167. https://doi.org/10.1016/10402004.2013.831962

Satyanarayana T, Rao P S, Krishna M G, (2019) Influence of wear parameters on friction performance of A 356 aluminium -graphite/granite particles reinforced metal matrix hybrid composites. Heliyon. 5(2019): e01770. https://doi.org/10.1016/j.heliyon.2019.e01770

Selvam JDR, Dinaharan I, Rai RS (2021) Matrix and reinforcement materials for metal matrix composites. In Book: Encyclopedia of Materials: Composites Publisher Elsevier. https://doi.org/10.1016/B978-0-12-803581-8.11890-9

Senapati AK, Sahoo SK, Singh S, Sah S, Padhi PR, Satapathy N (2017) A comparative investigation on physical and mechanical properties of MMC reinforced with waste materials. Int J Eng Adv Technol 6(4):161–169

Shaikh MBN, Arif S, Aziz T, Waseem A, Shaikh MAN, Ali M (2019) Microstructural, mechanical and tribological behaviour of powder metallurgy processed SiC and RHA reinforced Al-based composites. Surfaces Interfaces. https://doi.org/10.1016/j.surfin2019.03.002

Sharma VK, Singh RC, Chaudhary R (2017) Effect of flyash particles with aluminium melt on the wear of aluminium metal matrix composites. Eng Sci Technol Int J 20(2017):1318–1323. https://doi.org/10.1016/j.jestch.2017.08.004

Shihab SK, Gattmah J, Kadhim HM (2021) Experimental investigation of surface integrity and multi-objective optimization of end milling for hybrid Al7075 matrix composites. SILICON 13:1403–1419. https://doi.org/10.1007/s12633-020-00530-1

Shin S, Park H, Park B, Lee SB, Lee SK, Kim Y, Cho S, Jo I (2021) Dispersion mechanism and mechanical properties of SiC reinforcement in aluminium matrix composite through stir and die casting processes. Appl Sci 11(952):1–13. https://doi.org/10.3390/app11030952

Shreyas PS, Mahesh BP, Rajanna S, Rajesh N (2021) Evaluating the tribological properties of aluminium base hybrid composites reinforced with Al_2O_3 and ZrO_2 nano particles. Mater Today 45(2021):427–433. https://doi.org/10.1016/j.matpr.2020.12.1012

Simsek B, Tansel YI, Simsek EH (2015) A RSM-based multi-response optimization application for determining optimal mix proportions of standard ready-mixed concrete. Arab J Sci Eng. https://doi.org/10.1007/s13369-015-1987-0

Subrahmanyam APSVR, Madhukiran J, Naresh G, Madhusudhan S (2016) Fabrication and characterization of Al356.2, rice husk ash and fly ash reinforced hybrid metal matrix composite. Int J Adv Sci Technol. 94(2016): 49–56. https://doi.org/10.14257/ijast.2016.94.05

Subramaniam B, Natarajan B, Kaliyaperumal B, Jerold S, (2018). Investigation on mechanical properties of aluminium 7075-boron carbide-coconut shell-fly ash reinforced hybrid metal matrix composites. 15(6): 449–456. https://doi.org/10.1007/s41230-018-8105-3

Sun Y, Li C, Liu Y, Li H (2017) Intermetallic phase evolution and strengthening effect of Al-Mg-Si alloys with different Cu/Ni ratios. Mater Lett. https://doi.org/10.1016/j.matlet.2017.12.067

Swamy ARK, Ramesha A, Kumar GBV, Prakash JN (2011) Effect of particulate reinforcement on the mechanical properties of Al6061-WC and Al6061-Gr MMCs. J Min MaterCharacterization Eng 10(12):1141–1152

Sydow Z, Sydow M, Wojciechowski L, Bienczak K, (2021) Tribological performance of composites reinforced with the agricultural, industrial and post-consumer wastes: a review. 14(8): 1863. https://doi.org/10.3390/ma14081863.

Tash MM, Mahmond ERI, (2016) Development of in-situ/CuAl2 metal matrix composites: Microstructure, hardness and wear behavior. Materials. 9(442): 1–15. https://doi.org/10.3390/ma9060442

Tripathi A, Tyagi VK, Vivekanand V, Bose P, Suthar S (2020) (2020) Challenges, opportunity and progress in solid waste management during COVID-19 pandemic. Case Stud Chem Environ Eng 2:1000060. https://doi.org/10.1016/j.cscee.2020.1000060

Udoye N E, Nnamba O. J, Fayomi O S I, Inegbenebor A O, Jolayemi K J, (2020). Analysis on mechanical properties of AA 6061/rice husk ash composites produced through stir casting technique. Materials Today: Proceedings. https://doi.org/10.1016/j.matpr.2020.09.178

Usman AM, Raji A, Hassan MA, Waziri NH (2014b) A comparative study on the properties of Al-7% Si-rice husk ash and Al-7%Si-bagasse ash composites produced by stir casting. Int J Eng Sci 3(8):1–7

Usman A M, Raji A, Waziri NH, Hassan MA, (2014a) Aluminium alloy—rice husk ash composites production and analysis. Leonardo Electronic Journal of Practices and Technologies. (25): 84–98. https://lejpt.academicdirect.org

Venkatesh L, Arjunan TV, Ravikumar K, (2019) Microstructural characteristics and mechanical behaviour of aluminium hybrid composites reinforced with groundnut shell ash and B_4C. 41: 295. https://doi.org/10.1007/s40430-019-1800-1

Verma N, Vettivel SC (2018) Characterization and experimental analysis of boron carbide and rice husk ash reinforced AA7075 aluminium alloy hybrid composite. J Alloys Compounds 741(2018):981–998. https://doi.org/10.1016/j.jallcom.2018.01.185

Vijaya DJ, Pradeep JK, Smart DSR (2021) Analysis of hybrid aluminium composite material reinforced with Ti and NbC nano composites processed through stir casting. Materials Today. https10.1016/j.matpr.2021.05.683

Virkunwar AK, Ghosh S, Basak R, Rao AS, (2018) Study of mechanical and tribological characteristics of aluminium alloy reinforced with rice husk ash. Proceedings of TRIBOINDIA-2018, An International Conference on Tribology. https://doi.org/10.2139/ssrn.3313518.